

# Which Dominates Industrial-Current-Density CO<sub>2</sub>-to-C<sub>2+</sub> Electroreduction: Cu<sup>δ+</sup> or Microenvironment

Ruouo Yang,<sup>a</sup> Mao Wu,<sup>a</sup> Danji Huang,<sup>b</sup> Yan Yang,<sup>c</sup> Yan Liu,<sup>c</sup> Leiqian Zhang,<sup>d</sup> Feili Lai,<sup>e</sup>

Bo You,<sup>f</sup> Jiakun Fang,<sup>b</sup> Tianxi Liu,<sup>d</sup> Youwen Liu<sup>\*a</sup> and Tianyou Zhai<sup>\*a</sup>

<sup>a</sup>State Key Laboratory of Materials Processing and Die & Mould Technology, School of Materials Science and Engineering, Huazhong University of Science and

Technology, Wuhan, Hubei, 430074, P. R. China. E-mail: zhaity@hust.edu.cn;

ywliu@hust.edu.cn

<sup>b</sup>State Key Laboratory of Advanced Electromagnetic Engineering and Technology,

School of Electrical and Electronic Engineering, Huazhong University of Science and

Technology, Wuhan, Hubei, 430074, P. R. China.

<sup>c</sup>College of Chemistry and Materials Science, Anhui Normal University, Wuhu, Anhui,

241000, P. R. China.

<sup>d</sup>Key Laboratory of Synthetic and Biological Colloids, Ministry of Education, School of

Chemical and Material Engineering, Jiangnan University, Wuxi, Jiangsu, 214122, P. R.

China.

<sup>e</sup>Department of Chemistry, KU Leuven Celestijnenlaan, 200F, Leuven 3001, Belgium.

<sup>f</sup>Key Laboratory of Material Chemistry for Energy Conversion and Storage, Ministry

of Education, Hubei Key Laboratory of Material Chemistry and Service Failure, School

of Chemistry and Chemical Engineering, Huazhong University of Science and

Technology, Wuhan, Hubei, 430074, P. R. China.

## Experimental Section

**Chemicals.** Copper sulfate pentahydrate ( $\text{CuSO}_4 \cdot 5\text{H}_2\text{O}$ , 99%), ammonium hydroxide ( $\text{NH}_4\text{OH}$ , 25-28%), sodium hydroxide ( $\text{NaOH}$ , 96%), basic copper carbonate ( $\text{Cu}_2(\text{OH})_2\text{CO}_3$ , 99%) were purchased from Sinopharm Chemical Reagent Co., Ltd (Shanghai, China). All chemicals were used directly without further purification. Aqueous solutions were prepared using deionized water with a resistivity of  $18.2 \text{ M}\Omega \text{ cm}^{-1}$ .

**Materials Synthesis.** Synthesis of  $\text{Cu}_2(\text{OH})_2\text{CO}_3$  nanoparticles. Firstly, 1.6 mmol copper sulfate pentahydrate was dissolved in 40 ml of deionized water, and then 40 ml of 0.15 M ammonium hydroxide was dropwise added. After magnetic stirring for 30 min, 20 ml of 1.0 M sodium hydroxide was quickly added into the homogenous solution. After that, pure  $\text{CO}_2$  gas (Xiang Yun Supply) was aerated into the blue suspension with the  $20 \text{ ml min}^{-1}$  gas flow rate for 12 h. The precipitate was washed three times using deionized water via centrifugation and dried in a vacuum at  $60 \text{ }^\circ\text{C}$  for 12 h to obtain  $\text{Cu}_2(\text{OH})_2\text{CO}_3$  nanoparticles. Feeding can be scaled up by enlarging an equal proportion with the delay of pure  $\text{CO}_2$  gas inlet time.

**Characterization.** The samples were characterized by X-ray diffractometer (D2 PHASER, Bruker,  $\text{Cu K}\alpha$ ,  $\lambda = 1.5405 \text{ \AA}$ ), X-ray photoelectron spectroscopy (AXIS-ULTRA DLD-600W), SEM (FEI quanta650) and high-resolution transmission electron microscopy (FEI Tecnai G2 F30) with an X-ray energy dispersive spectrometer (EDS).

**In situ Raman Spectroscopy.** In situ Raman measurements were collected in a custom-built Raman cell in a confocal Raman spectroscopy (Alpha300, WITec) by using a 633

nm laser source. The laser power was kept at 2 mW and the integration times were 60 s. The electrolyte was 1.0 M KOH and 0.5 M K<sub>2</sub>SO<sub>4</sub> (pH adjusted to 1.6 with sulfuric acid) with a flow rate of 5 ml min<sup>-1</sup> and the CO<sub>2</sub> gas flow rate was 40 ml min<sup>-1</sup>. Before the experiment, calibration was performed according to the peak of the silicon wafer standard at 520 cm<sup>-1</sup>. Catalyst ink (500 μL) was sprayed into the 1 cm<sup>2</sup> gas diffusion layer (GDL, YLS-30T) as the working electrode. Ag/AgCl and carbon rod as the reference electrode and counter electrode, respectively. In situ spectroelectrochemistry was performed using a CHI 1140C workstation (CH instrument, Shanghai, China).

**Quasi in situ sXAS Spectroscopy.** Quasi in situ sXAS measurement was obtained at the BL12B beamline of National Synchrotron Radiation Laboratory (NSRL, China) under a total electron yield (TEY) mode with vacuum better than  $5 \times 10^{-7}$  Pa. The CuO<sub>x</sub>-dendrites catalyst was obtained by activating in the flow cell for 10 minutes with the CO<sub>2</sub> gas flow rate was 20 ml min<sup>-1</sup> at -0.4 V<sub>RHE</sub>. After activation, the GDL surface electrolyte was quickly removed and transferred to a vacuum test chamber.

**Operando XAFS Measurement.** Operando XAFS at Cu K-edge was collected in a custom-built XAFS flow cell at BL11B beamline by fluorescence mode at Shanghai Synchrotron Radiation Facility (SSRF). The beam current of the storage ring was 220 mA with a top-up mode. The incident photons were monochromatized by a Si (111) double crystal monochromator, with an energy resolution  $\Delta E/E \sim 1.4 \times 10^{-4}$ . The spot size at the sample was  $\sim 200 \mu\text{m} \times 200 \mu\text{m}$  (H  $\times$  V). All operando fluorescence mode measurements were using a custom flow cell (Figure S14). The window of the sample

equipment was mounted at an angle of approximately  $45^\circ$  with the incident beam and Lytle detector, which minimizes elastic scattering into the detector and maximizes the signal from the sample. The window facing the sample is sealed by Kapton tape. Catalyst ink (500  $\mu\text{L}$ ) was sprayed into the  $1\text{ cm}^2$  gas diffusion layer (GDL, YLS-30T) as the working electrode. Ag/AgCl and Pt net as the reference electrode and counter electrode, respectively. The electrolyte was 1.0 M KOH and 0.5 M  $\text{K}_2\text{SO}_4$  (pH adjusted to 1.6 with sulfuric acid) with a flow rate of  $5\text{ ml min}^{-1}$  and the  $\text{CO}_2$  gas flow rate was  $40\text{ ml min}^{-1}$ .

All measurements were made at room temperature in the fluorescence mode using Lytle detector with filled with argon gas in the ion chamber. To perform the evolution of structure, the scanning time was 3 min for collecting XANES from 8879 to 9179 eV. The XAFS energy range of Cu K-edge was collected from 8779 to 9779 eV about 15 min under each potential.

The raw data analysis was performed using the IFEFFIT software package according to the standard data analysis procedures.<sup>1</sup> To exclude self-absorption correction for fluorescence measurements, Booth algorithm was considered before fitting and the thickness of the samples were  $\sim 5.0\text{ }\mu\text{m}$ .<sup>2</sup>

**Electrochemical Measurements.** The  $\text{CO}_2$  electrochemical reduction reaction was conducted in a flow cell with a standard three-electrode system controlled by a CHI 1140C workstation (CH instrument, Shanghai, China). The catalyst ink was prepared, and 10 mg catalyst was dispersed in 50  $\mu\text{L}$  Nafion solution (5%) in 950  $\mu\text{L}$  isopropanol-water solution in a 3:1 volume ratio by ultrasonic dispersion with 15 min to form a

homogeneous ink. The catalyst ink was sprayed into the gas diffusion layer (GDL, YLS-30T) as the working electrode, Ag/AgCl (saturated KCl) electrode as the reference electrode, and Pt net as the counter electrode. For the flow cell, the catalyst ink was deposited on the 1 cm<sup>2</sup> of gas diffusion layer as the working electrode. The flow-cell measurements were conducted in 1 M KOH and 0.5 M K<sub>2</sub>SO<sub>4</sub> (pH adjusted to 1.6 with sulfuric acid) with a CO<sub>2</sub> flow rate of 40 ml min<sup>-1</sup>. Each performance test was repeated three times. Quantification of gas products detected by an in-situ gas chromatograph (PANNA, A91lus). The liquid products were conducted by nuclear magnetic resonance (NMR) spectrometer (Bruker Ascend™ 600 MHz). All the potentials were switched to values with reference to the RHE using:

$$E_{RHE} = E_{Ag/AgCl} + 0.197V + 0.0591 \times pH$$

To offset the ohmic loss, 85% iR compensation (i, current; R, uncompensated resistance) was applied to correct the potentials manually.

FE for each product was calculated from the equation below:

$$FE_g = \frac{z_g x_g F}{Q} \times 100$$

where  $z_g$  is the number of electrons transferred for gas,  $x_g$  is the number of moles of gas,  $F$  is Faraday's constant (96485 C·mol<sup>-1</sup>) and  $Q$  is the integrated charge.

SPCE was calculated from the equation below:

$$SPCE = \frac{60 s \times \sum (I \times x_g \times FE_g \div (N_g \times F))}{f \times 1 \text{ min} \div 24.5}$$

where  $I$  is the applied current,  $x_g$  is mole ratio of CO<sub>2</sub> to a specific product,  $FE_g$  is the FE of a specific group of products from CO<sub>2</sub>R,  $f$  is the gas flow rate and  $N_g$  is the number

of electron transfers for every specific product.

**COMSOL multiphysics simulations.** A two-dimensional finite element model was developed to describe the difference of current density distribution between dendrites electrode and particles electrode. A two-dimensional cross-section of  $130 \times 150$  nm near the electrode was taken for the computational domain. The dendrites electrodes are represented by specific tip, while the particles electrodes are assumed to be irregular grain. The secondary current distribution module from the COMSOL multiphysics software was selected to describe the current and potential distributions in the cell, while Butler-Volmer expression was further used to reveal the electrode kinetics of the charge transfer reaction at room temperature in the bulk electrolyte. Boundary conditions: The upper boundary was set as the electrolyte boundary with a current density at  $-100 \text{ mA cm}^{-2}$ . The electrolyte and electrode conductivity were assumed to be  $10 \text{ S/m}$  and  $1e^7 \text{ S/m}$ , respectively. Then, the electrical double layer was modeled using the Gouy-Chapman-Stern model to describe the difference of electric field distribution between plate electrode and square electrode, which consists of a Helmholtz layer and a diffusion layer. The former consists of a monolayer of surface-adsorbed hydrated  $\text{K}^+$  cation on the catalyst surface. The latter consisted of cations and anions, which is established as the result of a dynamic equilibrium between electrostatic forces and diffusion. In a steady state, the Poisson-Nerst-Planck equations could be solved to gain the electric field and  $\text{K}^+$  concentration near the catalyst surface. The diffusion coefficient  $D$  of the potassium and hydroxyl ion were taken to be  $2.14 \times 10^{-9} \text{ m}^2 \text{ s}^{-1}$  and  $6.8 \times 10^{-9} \text{ m}^2 \text{ s}^{-1}$  in water.

**DFT Calculations.** All the DFT calculations were performed with the Vienna ab initio simulation package (VASP).<sup>3,4</sup> The exchange-correlation function was described by the generalized gradient approximation (GGA) within the Perdew–Burke–Ernzerhof (PBE).<sup>5,6</sup> The projector augmented wave (PAW) method was used to account for core-valence interactions.<sup>7</sup> The vacuum layer was set as 15 Å to eliminate interplanar interactions. The kinetic cutoff energy for the plane-wave expansion of the electronic wave function was set as 450 eV. The Brillouin zone was sampled with a 3 × 3 × 1 k-mesh in the  $\Gamma$ -centered Monkhorst-Pack scheme.<sup>8</sup> The convergence criteria were set to be 0.02 eV/Å and  $1 \times 10^{-5}$  eV for the force on each atom and the total energy, respectively. The Grimme DFT-D3 scheme was adopted in the DFT calculations to describe the van der Waals (vdW) interactions. The 4×4 Cu(111) and 2×2 Cu<sub>2</sub>O(111) surface slabs were constructed with three layers and the bottom layer was fixed.

The change of the Gibbs free energy of each elemental step in the reaction pathway is based on the computational hydrogen electrode (CHE) model<sup>9</sup> with:

$$\Delta G = \Delta E_{\text{DFT}} + \Delta E_{\text{ZPE}} - T\Delta S$$

where  $\Delta E_{\text{DFT}}$ ,  $\Delta E_{\text{ZPE}}$ , and  $\Delta S$  correspond to the change of the calculated energy, the change of zero-point energy, and the change of entropy at room temperature (T = 298.15 K).

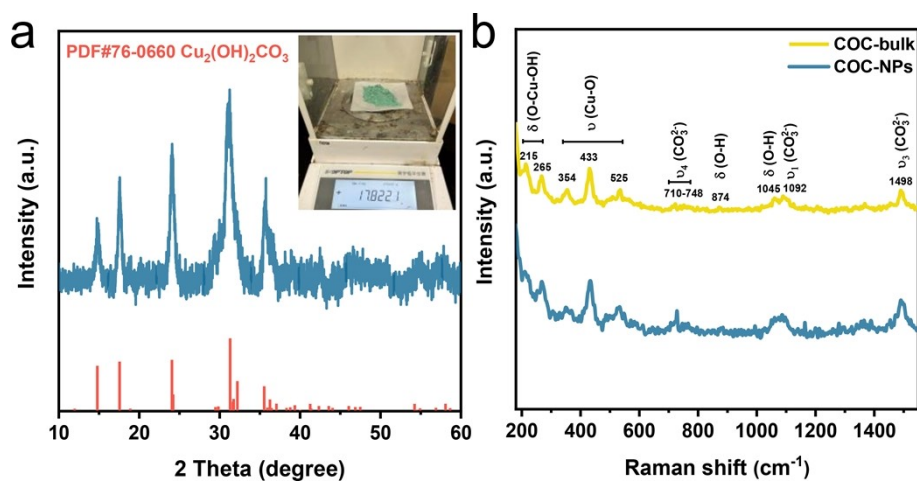


**Figure S1.** (a) XRD of  $\text{Cu}_2(\text{OH})_2\text{CO}_3$  nanoparticles. (b) Raman spectroscopy of  $\text{Cu}_2(\text{OH})_2\text{CO}_3$  nanoparticles and commercial  $\text{Cu}_2(\text{OH})_2\text{CO}_3$  bulk. Raman peaks at 215, 265  $\text{cm}^{-1}$  were represented to  $\delta(\text{O-Cu-OH})$  bend. 354, 433 and 525  $\text{cm}^{-1}$  were represented to  $\nu(\text{Cu-O})$  stretch. The bulge of 710-748  $\text{cm}^{-1}$  was represented to  $\nu_4(\text{CO}_3^{2-})$  stretch. 874 and 1045  $\text{cm}^{-1}$  were attributed to the  $\delta(\text{O-H})$  bend. 1092 and 1498  $\text{cm}^{-1}$  were attributed to the  $\nu_1(\text{CO}_3^{2-})$  and  $\nu_3(\text{CO}_3^{2-})$ , respectively.<sup>10,11</sup>

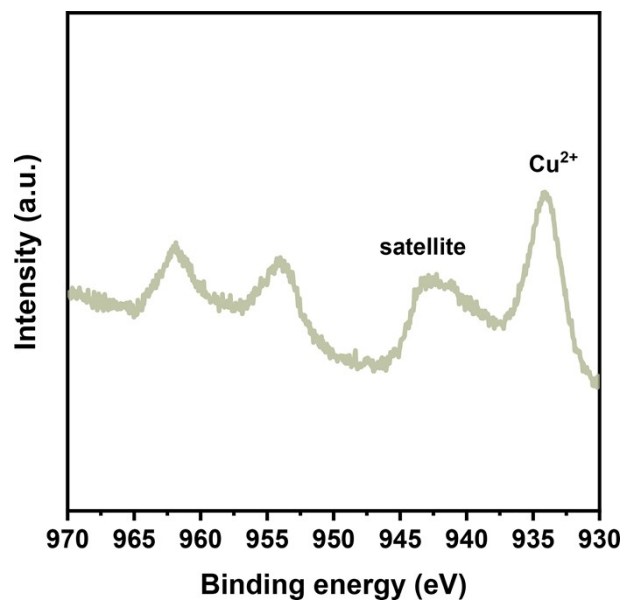


**Figure S2.** Cu 2p XPS results of  $\text{Cu}_2(\text{OH})_2\text{CO}_3$  nanoparticles.

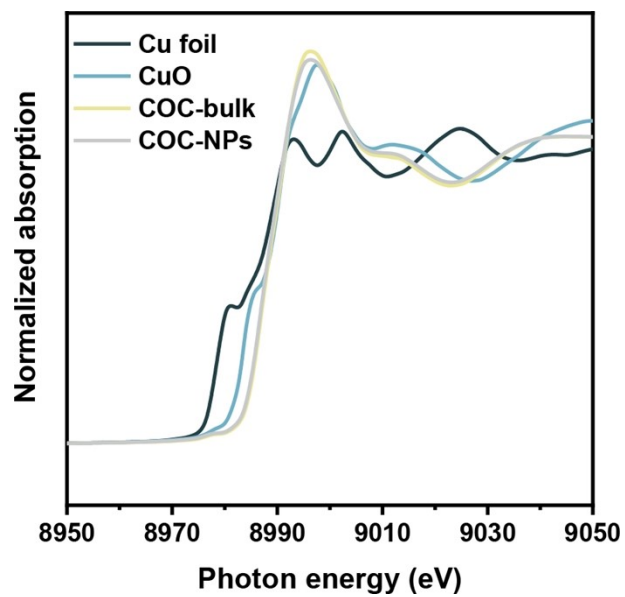


**Figure S3.** Cu K-edge XANES results of  $\text{Cu}_2(\text{OH})_2\text{CO}_3$  nanoparticles and commercial  $\text{Cu}_2(\text{OH})_2\text{CO}_3$ .

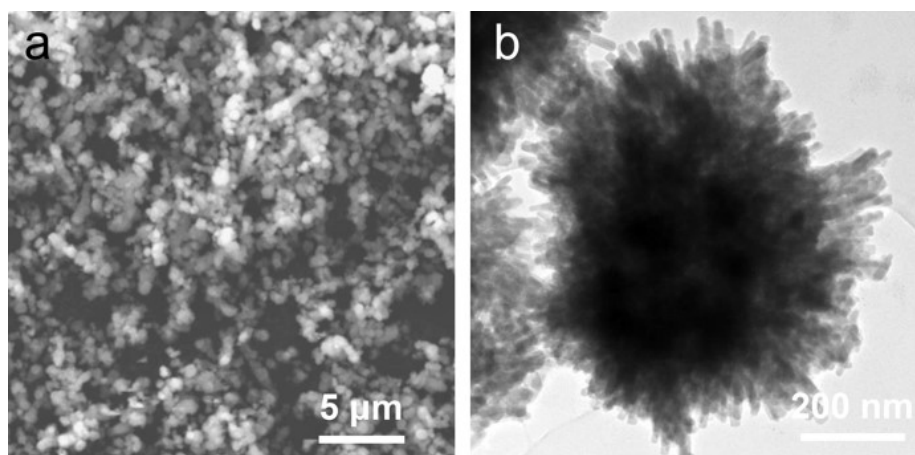


**Figure S4.** (a) SEM (b) TEM of  $\text{Cu}_2(\text{OH})_2\text{CO}_3$  nanoparticles.

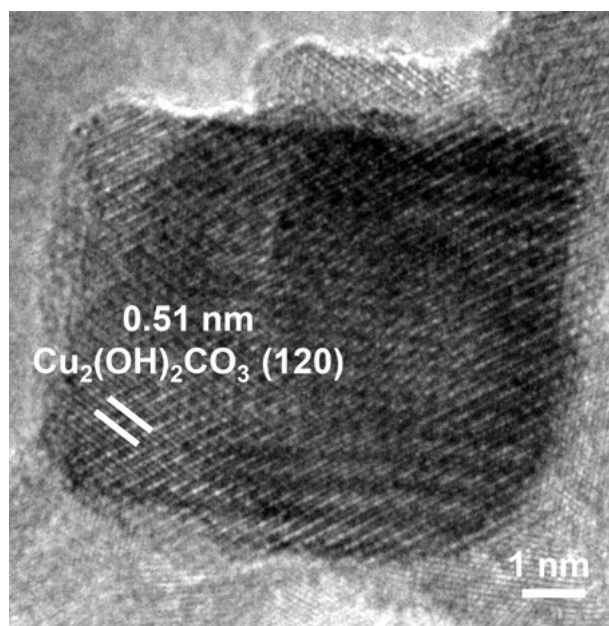


**Figure S5.** HRTEM images of  $\text{Cu}_2(\text{OH})_2\text{CO}_3$  nanoparticles.

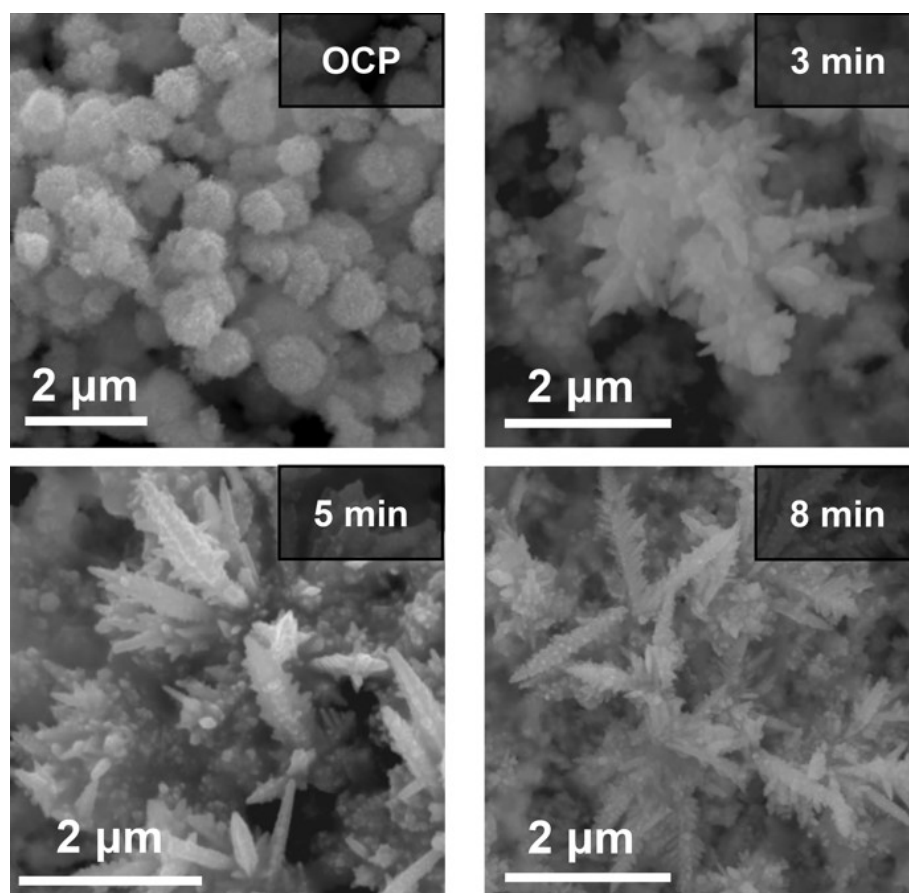


**Figure S6.** SEM images for  $\text{Cu}_2(\text{OH})_2\text{CO}_3$  nanoparticles during electrochemical reduction with time.

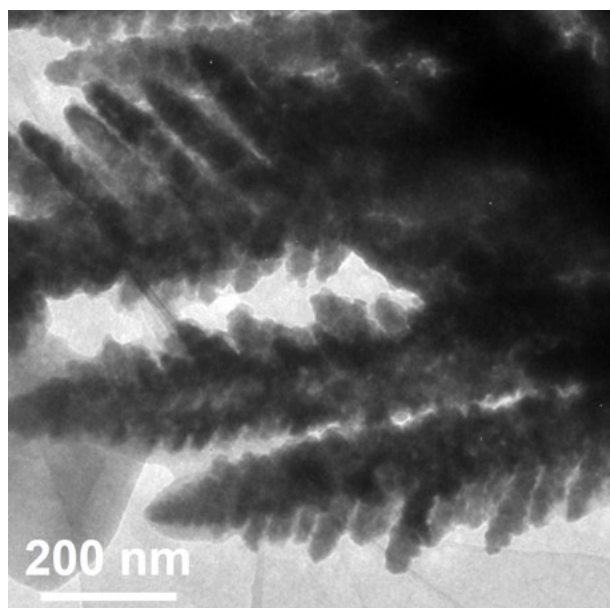


**Figure S7.** TEM image for COC-NPs after electrochemical reduction.

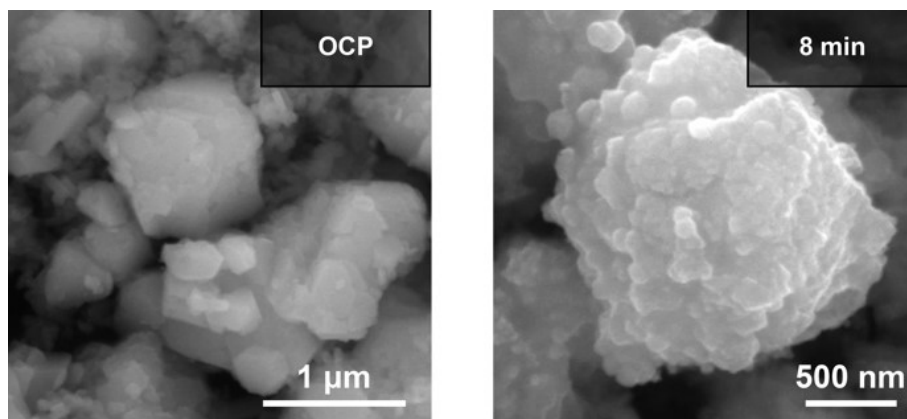


**Figure S8.** SEM images for commercial  $\text{Cu}_2(\text{OH})_2\text{CO}_3$  during electrochemical reduction.

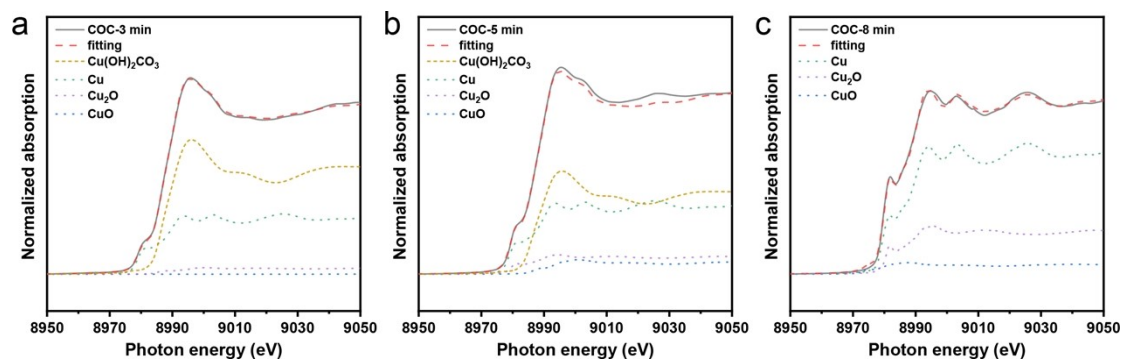


**Figure S9.** LCF of  $\text{Cu}_2(\text{OH})_2\text{CO}_3$  nanoparticles under  $-0.4 \text{ V}_{\text{RHE}}$  taken at 3 min (a), 5 min (b), and 8 min (c).

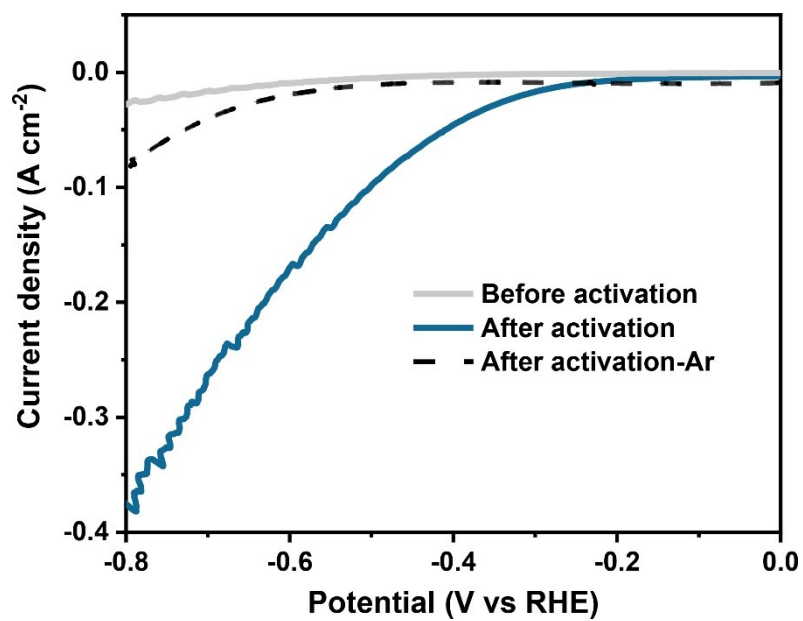


**Figure S10.** LSV curves for  $\text{Cu}_2(\text{OH})_2\text{CO}_3$  nanoparticles before activation and after activation with  $\text{CO}_2/\text{Ar}$  in 1.0 M KOH.

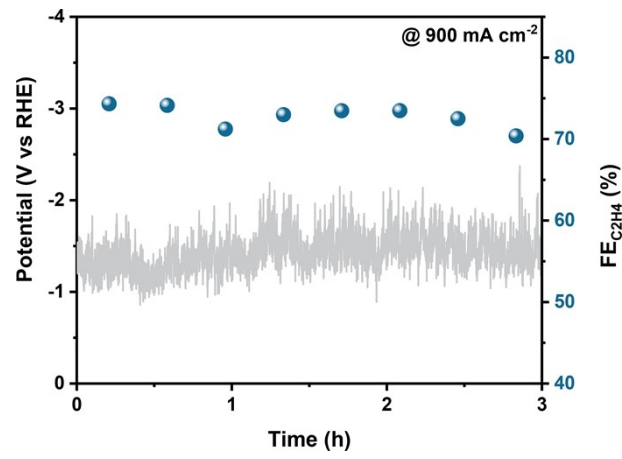


**Figure S11.** Stability test of CuO<sub>x</sub>-dendrites at the current density of 900 mA cm<sup>-2</sup>.

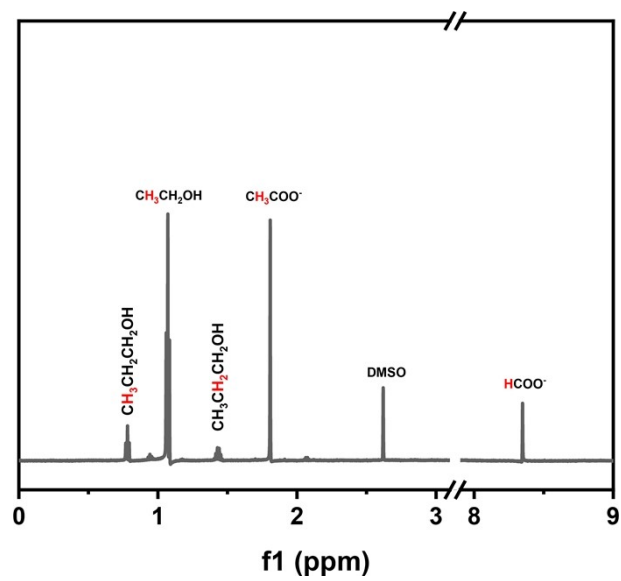


**Figure S12.**  $^1\text{H}$ -NMR spectrum of aqueous products formed using  $\text{CuO}_x$ -dendrites at a current density of  $900 \text{ mA cm}^{-2}$  after 3 h.

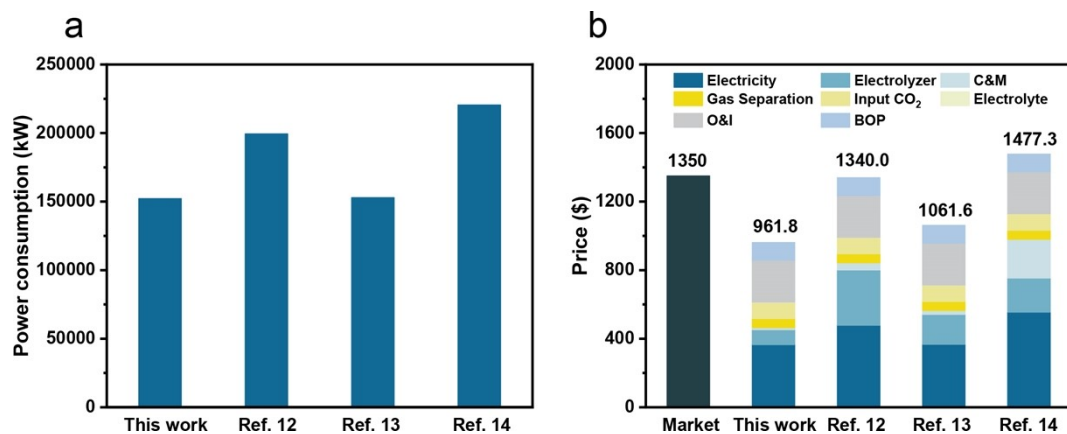


**Figure S13.** (a) The power consumption and (b) the market price and the subdivided cost of  $C_2H_4$  electrosynthesis by optimal performance of  $CuO_x$ -dendrites and state-of-the-art industrially catalysts with the given electricity price of  $USD\ 0.01\ kWh^{-1}$  by the theoretical limit single-pass carbon efficiency (SPCE) for alkaline systems<sup>12-14</sup>. The details were presented by Supplementary Note 1.

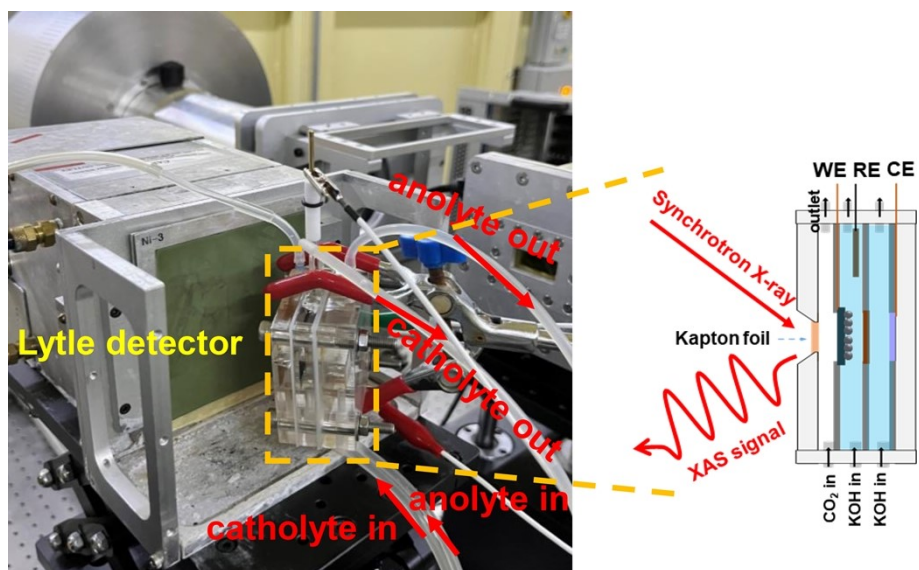


**Figure S14.** Photo and illustration of the operando XAFS test equipment. WE, RE, and CE represent the working electrode, reference electrode, and counter electrode, respectively.

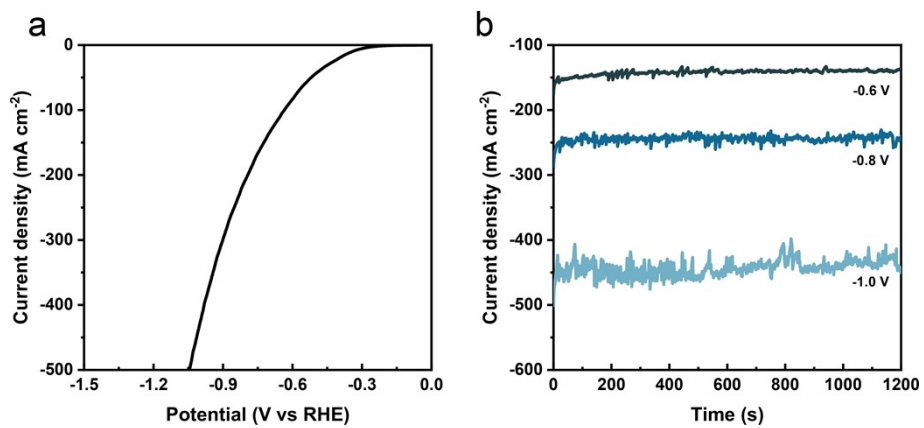


**Figure S15.** Electrochemical measurements in the operando XAFS test equipment. (a) LSV profiles of CuO<sub>x</sub>-dendrites in the XAFS test equipment, (b) Chronoamperometry (CV) profiles of CuO<sub>x</sub>-dendrites at -0.6, -0.8, and -1.0 V<sub>RHE</sub>.

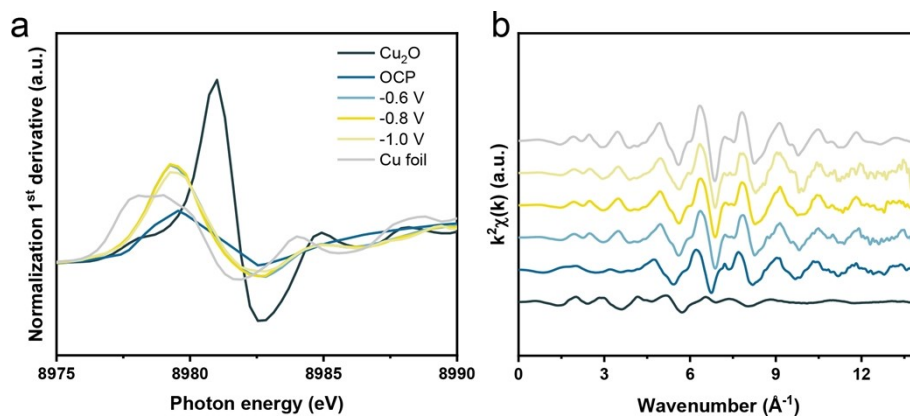


**Figure S16.** Operando Cu K-edge first derivative of XANES (a) and k space (b) of CuO<sub>x</sub>-dendrites during the CO<sub>2</sub>R.

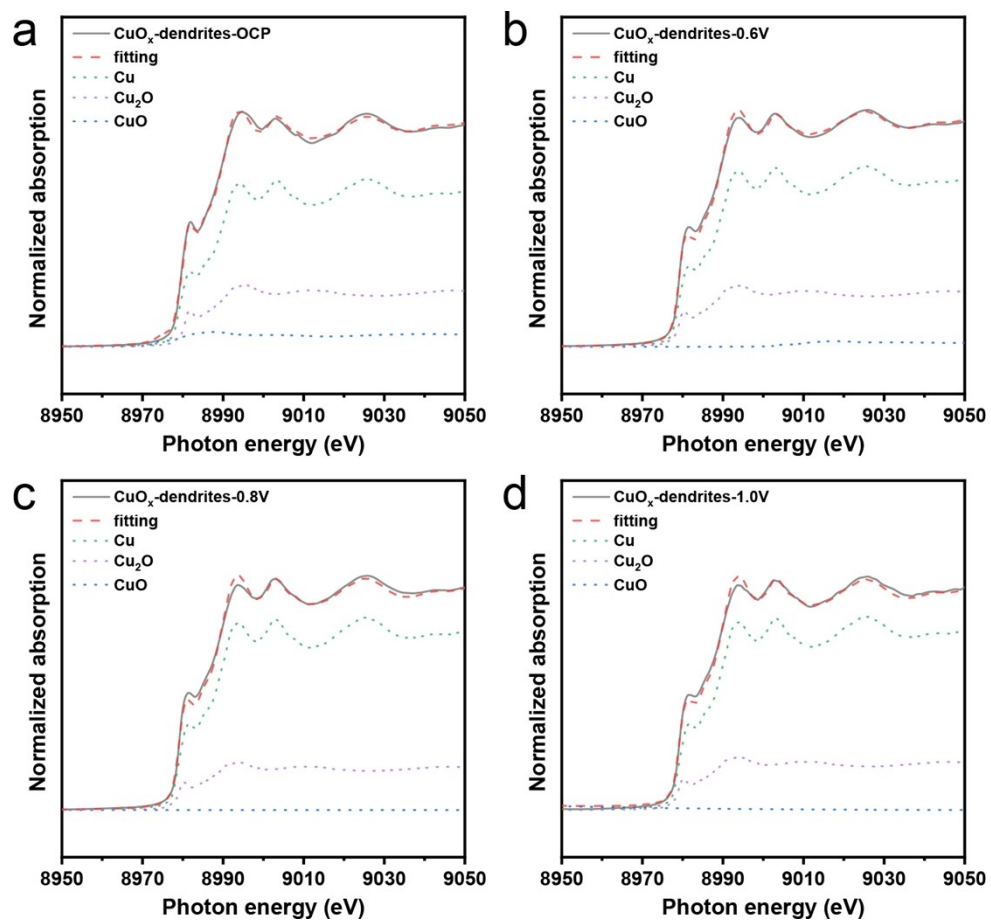


**Figure S17.** LCF of  $\text{CuO}_x$ -dendrites at OCP (a), -0.6 (b), -0.8 (c), and -1.0  $V_{\text{RHE}}$  (d).

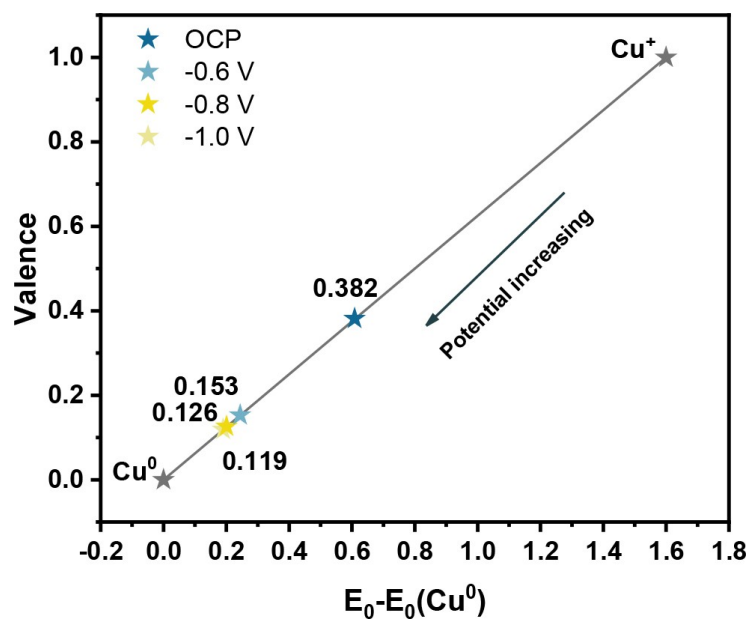


**Figure S18.** The average oxidation states fitted via XANES spectra of CuO<sub>x</sub>-dendrites. The absorption edge of CuO<sub>x</sub>-dendrites catalyst at OCP shifted 0.61 eV towards higher energy relative to that of Cu foil, corresponding to the Cu valence state +0.382 at OCP. The energy level gradually approached that of the Cu foil when the potential decreased from -0.6 V<sub>RHE</sub> to -1.0 V<sub>RHE</sub>, suggesting the further reduction of CuO<sub>x</sub>-dendrites. However, the valence state of Cu was +0.119 which indicated that the active Cu<sup>+</sup> species seem to be stable during the ICD-CO<sub>2</sub>R.

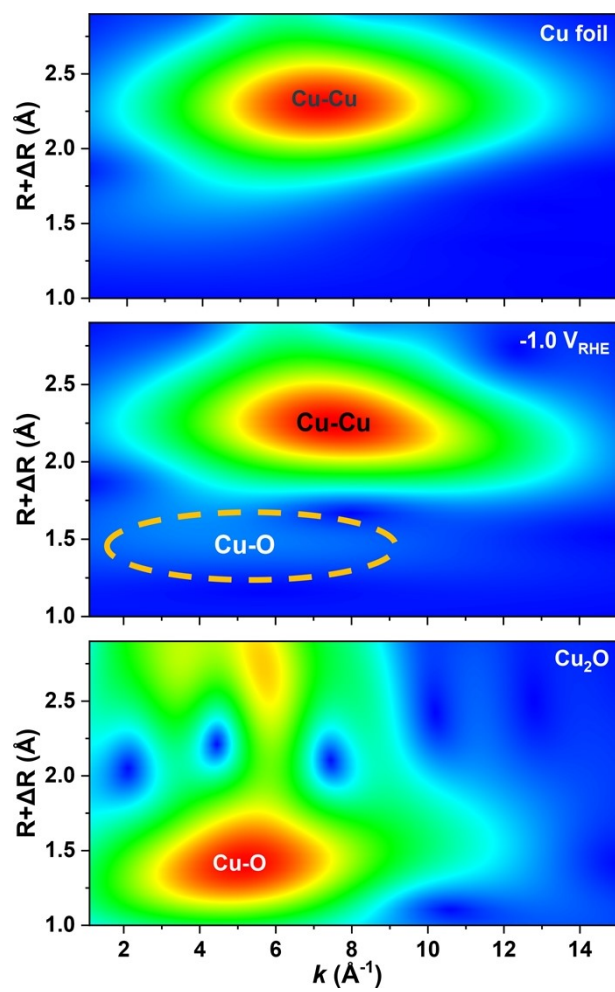


**Figure S19.** The WT-EXAFS at  $-1.0 V_{\text{RHE}}$  for  $\text{CuO}_x$ -dendrites and Cu foil,  $\text{Cu}_2\text{O}$  standard samples.

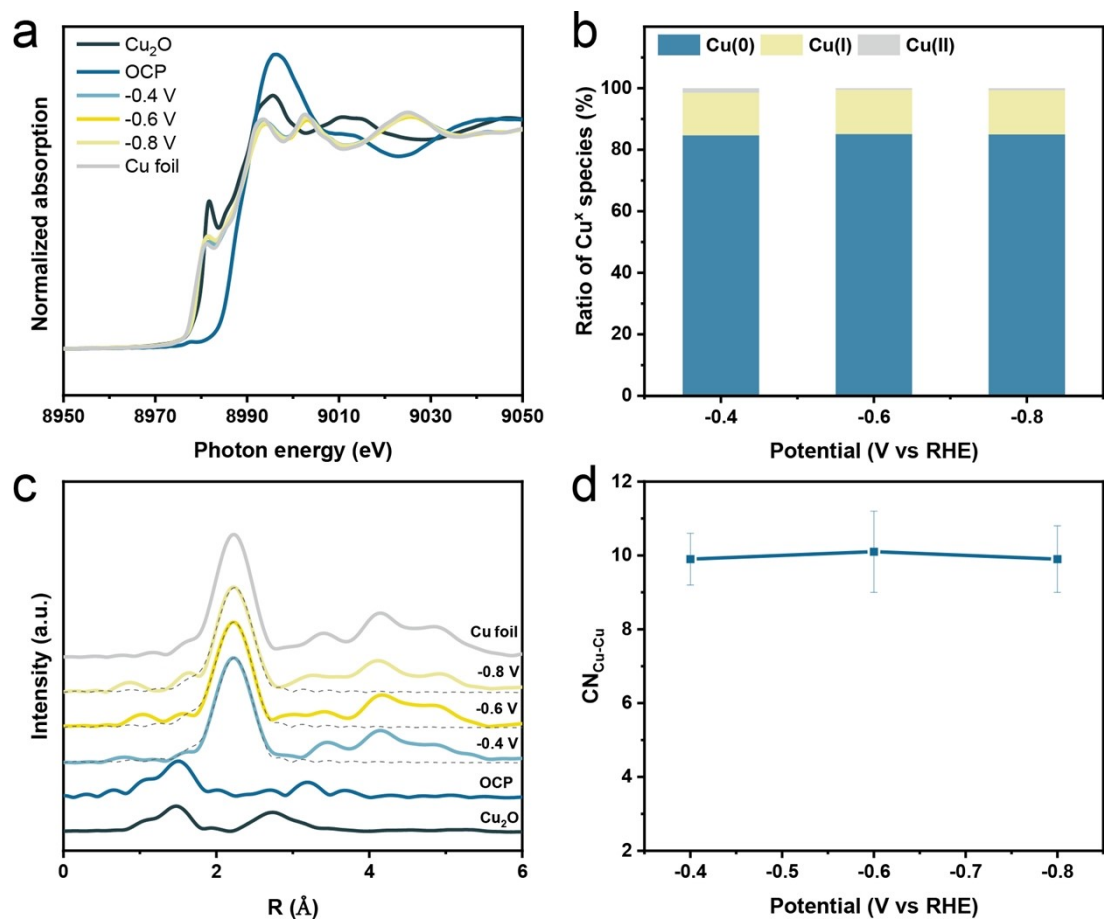


**Figure S20.** (a) Operando Cu K-edge XANES of CuO<sub>x</sub>-particles during the CO<sub>2</sub>R. (b) The calculated ratio of Cu<sup>x</sup> species concerning potential. (c) Fourier-transform k<sup>2</sup>-weighted EXAFS spectra. (d) Coordination numbers of the metallic Cu-Cu coordination shell at different potentials.

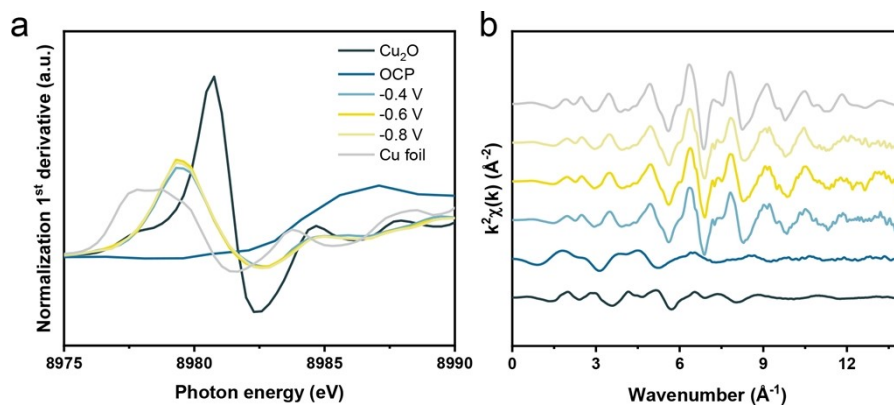


**Figure S21.** Operando Cu K-edge first derivative of XANES (a) and k space (b) of CuO<sub>x</sub>-particles during the CO<sub>2</sub>R.

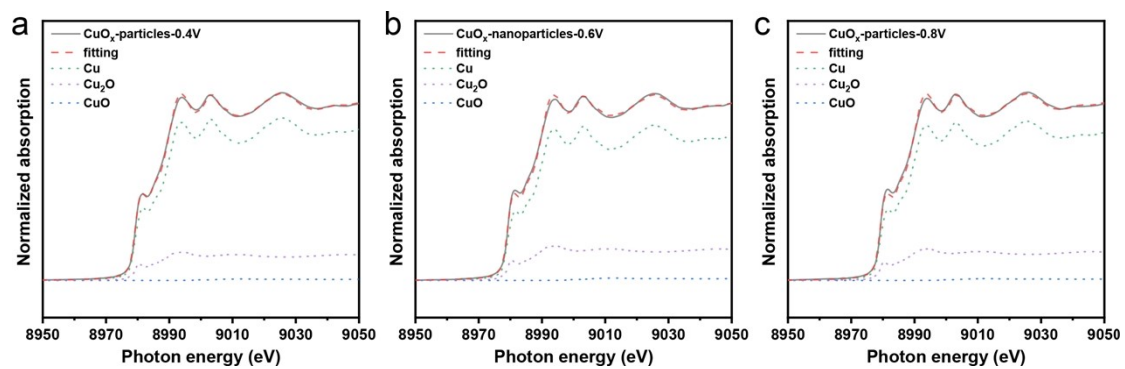


**Figure S22.** LCF of CuO<sub>x</sub>-particles at -0.4 (a), -0.6 (b), -0.8 V<sub>RHE</sub> (c).

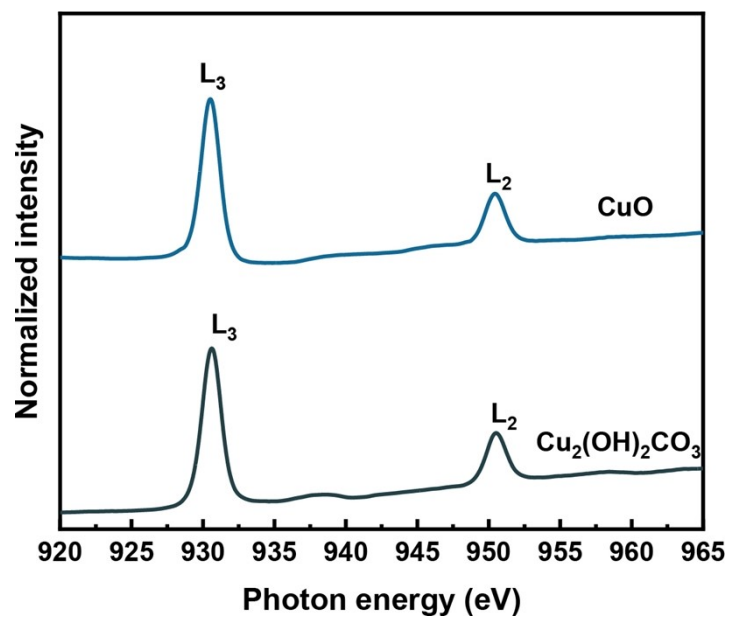


**Figure S23.** Cu L-edge soft X-ray absorption spectroscopy (sXAS) spectra for CuO standard and Cu<sub>2</sub>(OH)<sub>2</sub>CO<sub>3</sub> nanoparticles.

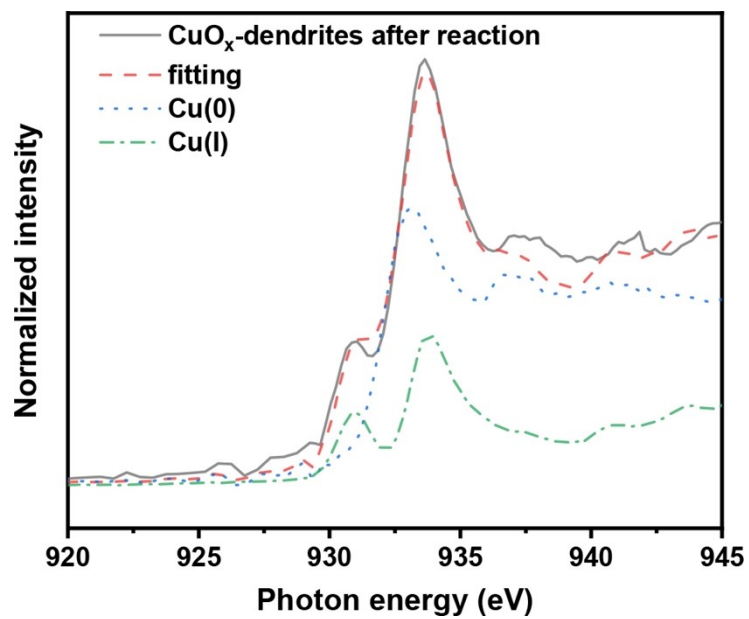


**Figure S24.** Linear combination of Cu L<sub>3</sub>-edge sXAS spectra for CuO<sub>x</sub>-dendrites after 1 h reaction at -1.0 V<sub>RHE</sub>.

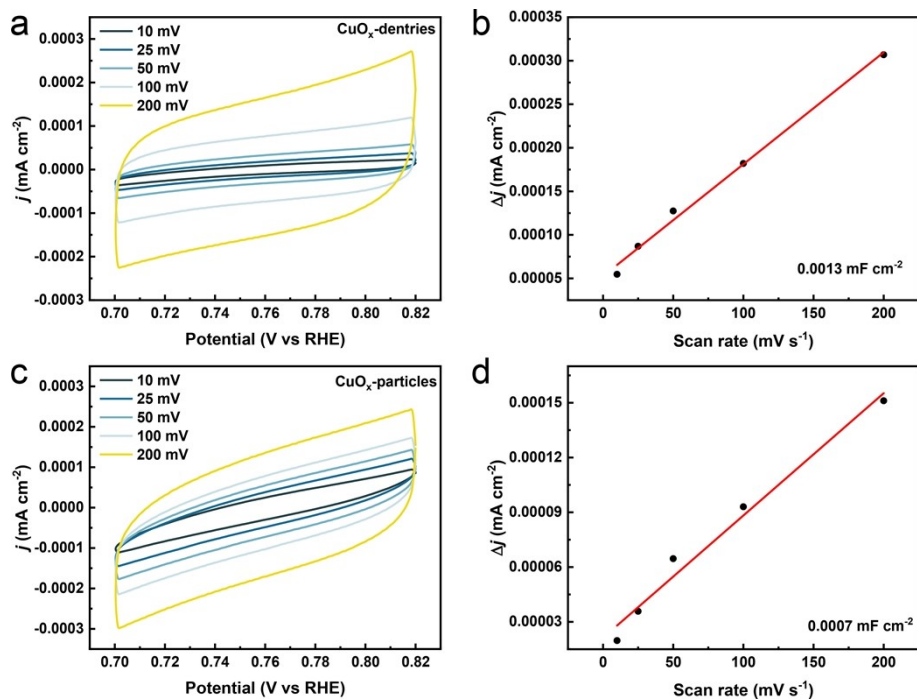


**Figure S25.** Cyclic voltammetry (CV) curves of CuO<sub>x</sub>-dendrites (a) and CuO<sub>x</sub>-particles (c) different scanning rates. Determination of double-layer capacitance over a range of scan rates (10, 25, 50, 100, and 200 mV s<sup>-1</sup>) for CuO<sub>x</sub>-dendrites (b) and CuO<sub>x</sub>-particles (d).

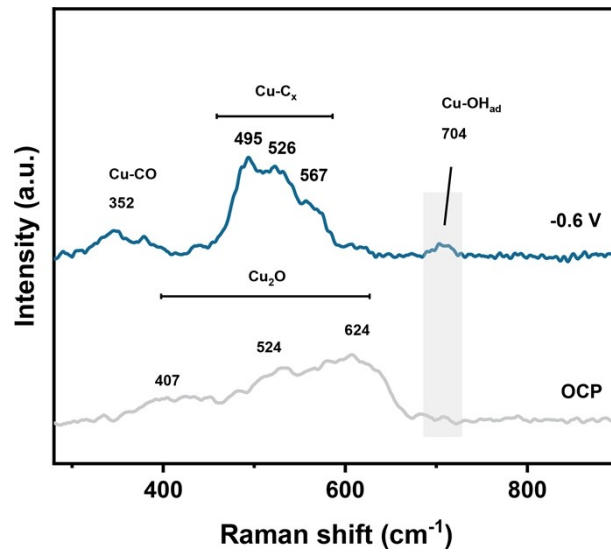


**Figure S26.** In situ Raman spectroscopy of  $\text{CuO}_x$ -particles at OCP and  $-0.6\text{ V}_{\text{RHE}}$ .

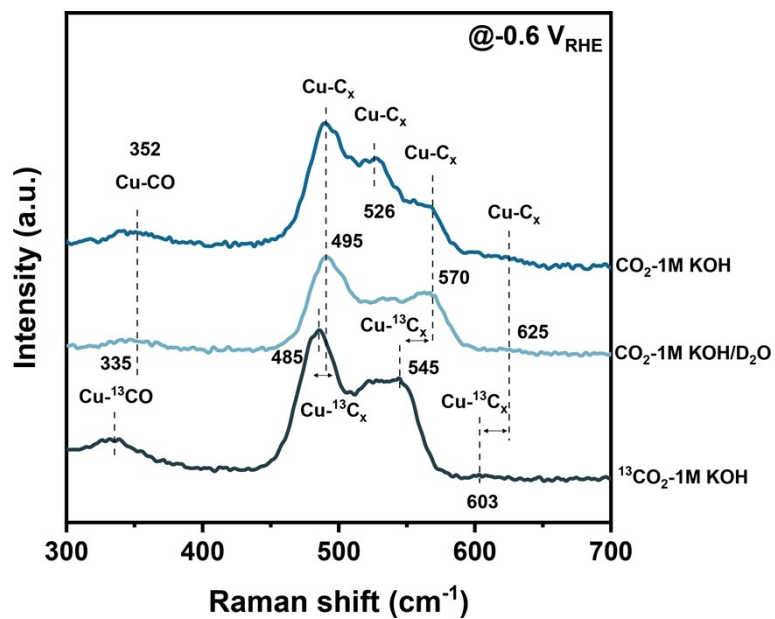


**Figure S27.** Isotope labeling ( $\text{D}_2\text{O}$  and  $^{13}\text{CO}_2$ ) in electrochemical in situ Raman spectroscopy. The peaks of 495, 526, 570, and 625  $\text{cm}^{-1}$  shifted to lower wavenumber by in situ Raman, which meant these peaks were connected with Cu-C<sub>x</sub> species rather than Cu-OH or Cu-O.

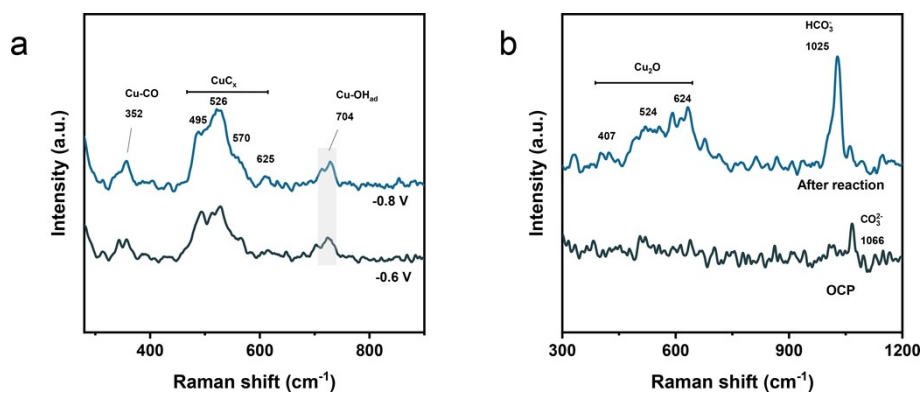


**Figure S28.** In situ Raman spectroscopy of Cu powder with potential applied (a) and OCP/after reaction (b) by 0.01M KOH. Similarly, a bulge peak of 704 cm<sup>-1</sup> which referred to Cu-OH<sub>ad</sub> was conducted during the reaction, which suggested that the hydroxide adsorption was universal under the negative potential applied. Moreover, when the voltage was removed, the Cu(0) powder was partially oxidized, which indicated the strong oxidation ability of the adsorption of hydroxide.

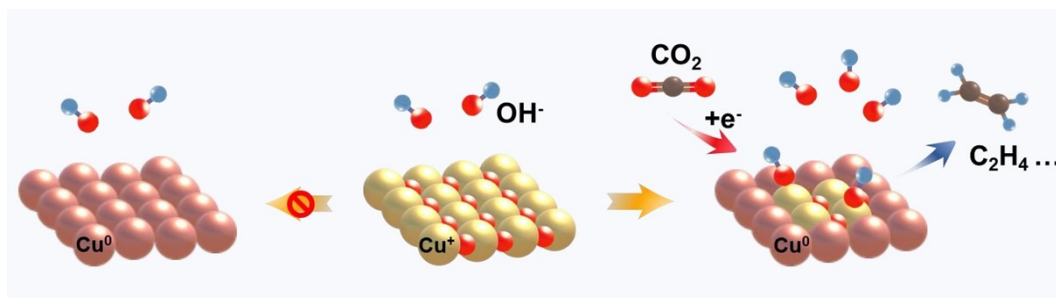


**Figure S29.** The hypothetical dynamic reduction process. The surface of catalysts will generate abundant hydroxyl species owing to the consumption of proton under the ICD- $\text{CO}_2\text{R}$ . The hydroxyl species with oxidation capacity dynamically prevented the reduction of catalysts<sup>15</sup>.

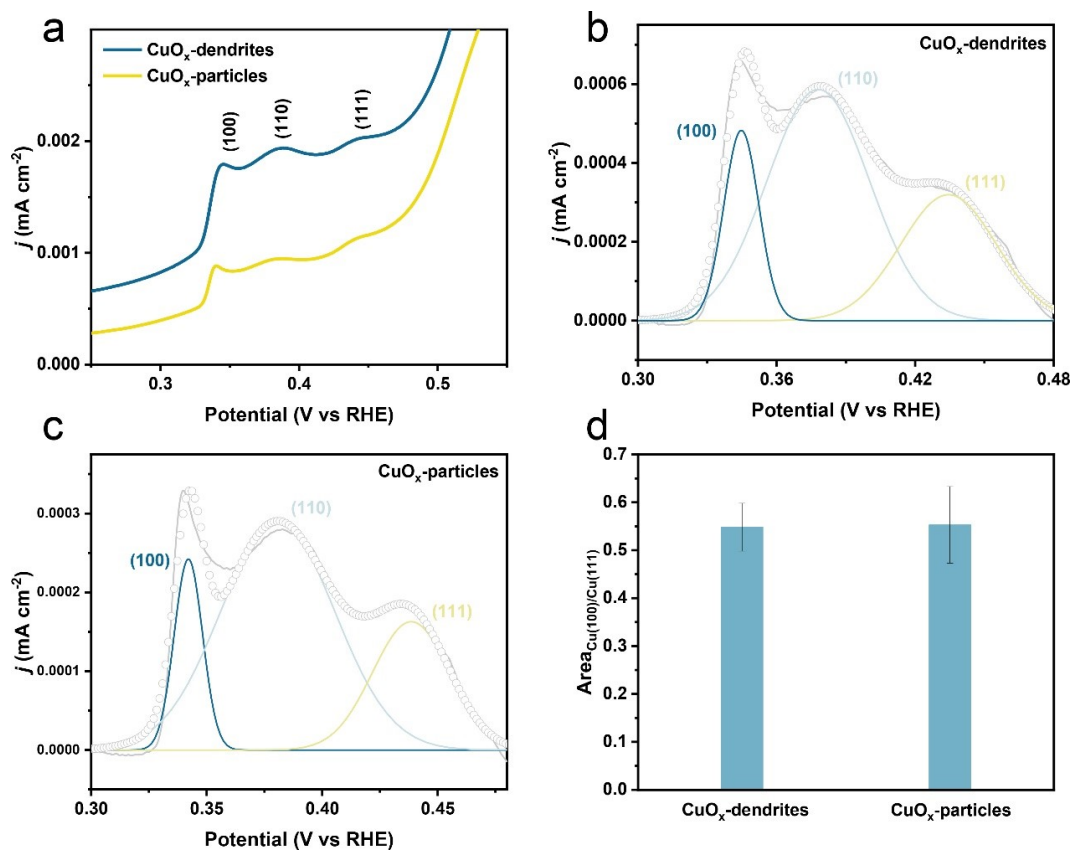


**Figure S30.** (a) Voltammogram curves of CuO<sub>x</sub>-dendrites and CuO<sub>x</sub>-particles with a sweep rate of 100 mV s<sup>-1</sup>. (b) Fitted OH<sup>-</sup> adsorption peaks of (b) CuO<sub>x</sub>-dendrites and (c) CuO<sub>x</sub>-particles. (d) Fitted OH<sup>-</sup> adsorption peaks quantified Cu(100)/Cu(111) area of CuO<sub>x</sub>-dendrites and CuO<sub>x</sub>-particles.

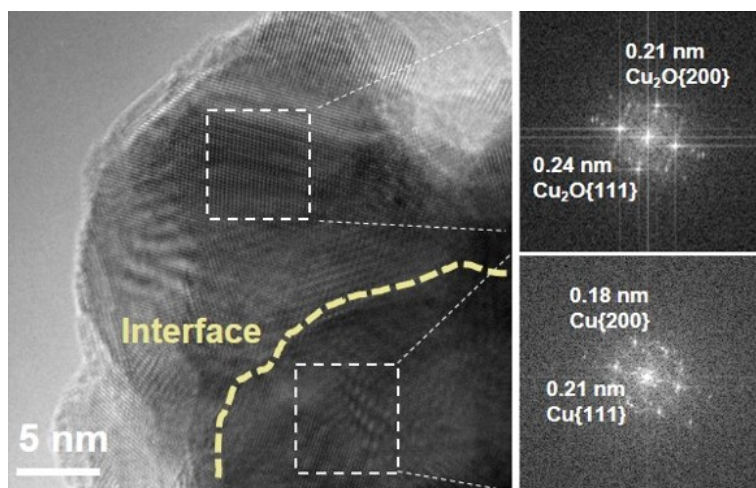


**Figure S31.** HRTEM image and corresponding fast Fourier Transform (FFT) diffraction patterns for Cu<sub>2</sub>O and Cu.

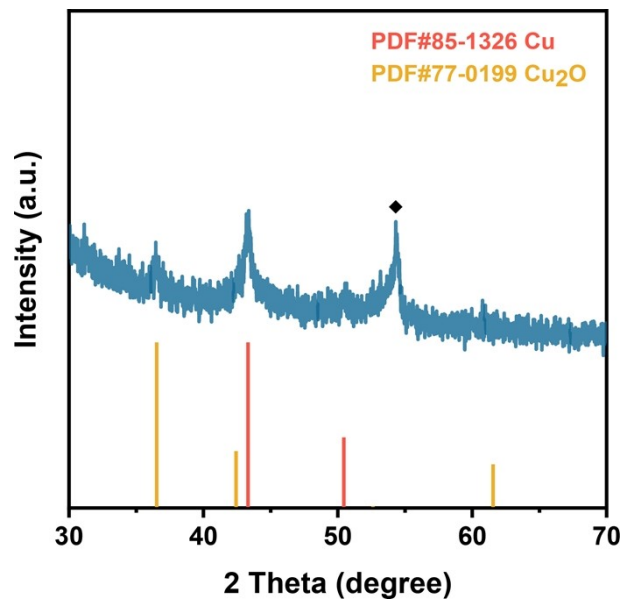


**Figure S32.** XRD of CuO<sub>x</sub>-dendrites. The black rhombus indicates a feature ascribed to GDE.

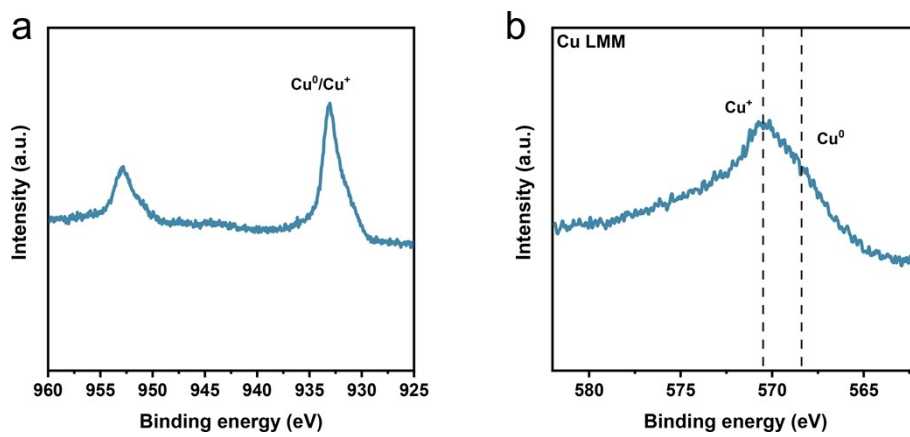


**Figure S33.** (a) Cu 2p XPS and (b) Cu LMM auger spectra of CuO<sub>x</sub>-dendrites.

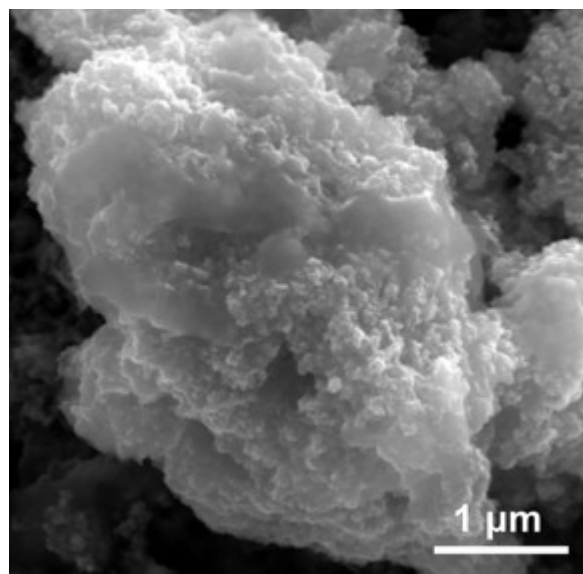


**Figure S34.** SEM image of CuO<sub>x</sub>-particles.

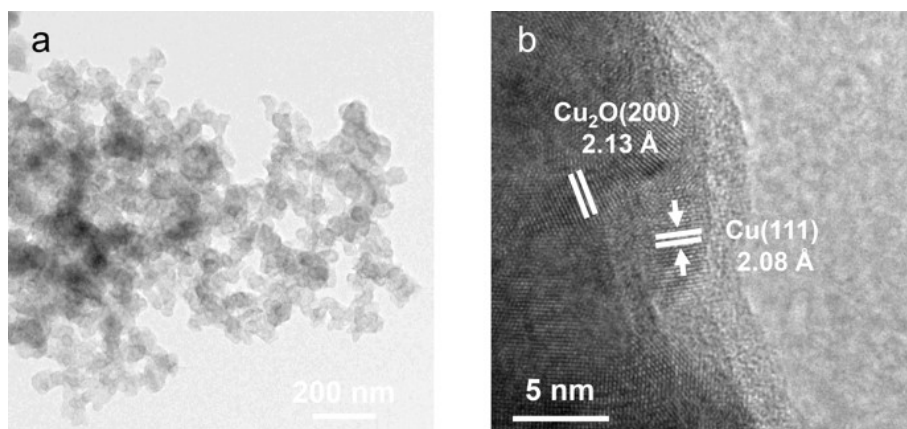


**Figure S35.** (a) TEM and (b) HRTEM images of  $\text{CuO}_x$ -particles.

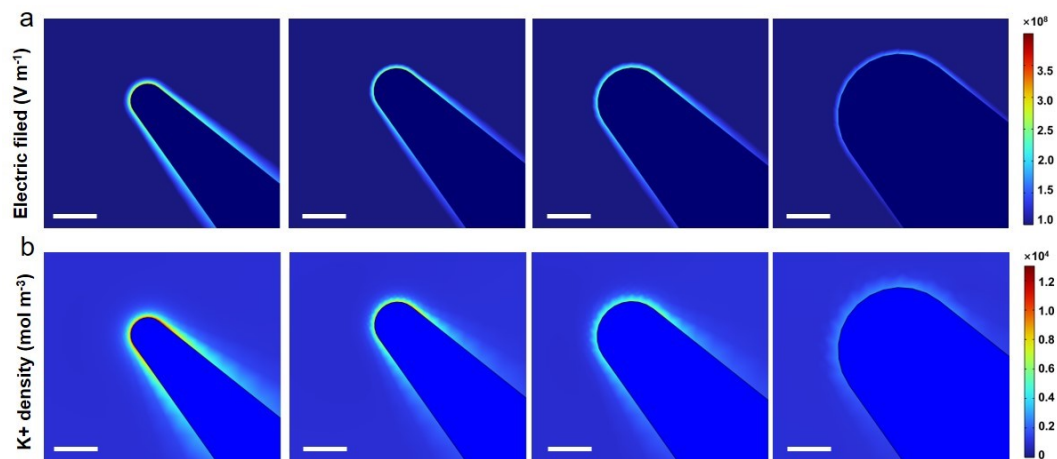


**Figure S36.** Simulated (a) electric field and (b) K<sup>+</sup> density distribution near the tip with different radius (1 to 4) of curvature. Scale bar, 5 nm.

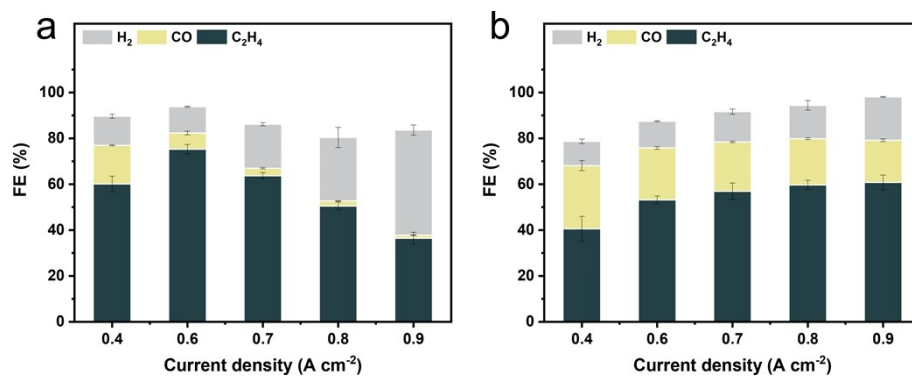


**Figure S37.** FE of gas products bias collected in a flow cell of CuO<sub>x</sub>-dendrites in (a) 2.50 M KOH and (b) 0.75 M KOH.

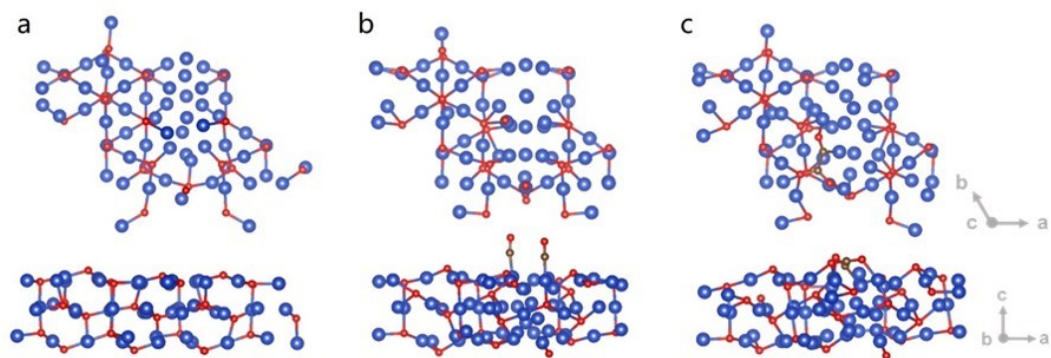


**Figure S38.** The DFT calculation models of (a)  $\text{CuO}_x$  and  $\text{CuO}_x$  for (b)  $\text{CO}^*+\text{CO}^*$  formation and (b)  $\text{O}^*\text{CCO}$  formation.

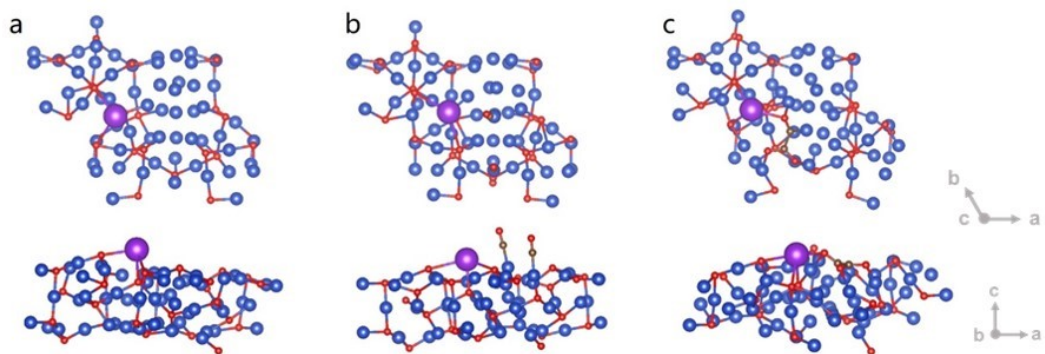


**Figure S39.** The DFT calculation models of (a)  $\text{CuO}_x+\text{K}^+$  and  $\text{CuO}_x+\text{K}^+$  for (b)  $\text{CO}^*+\text{CO}^*$  formation and (b)  $\text{O}^*\text{CCO}$  formation.

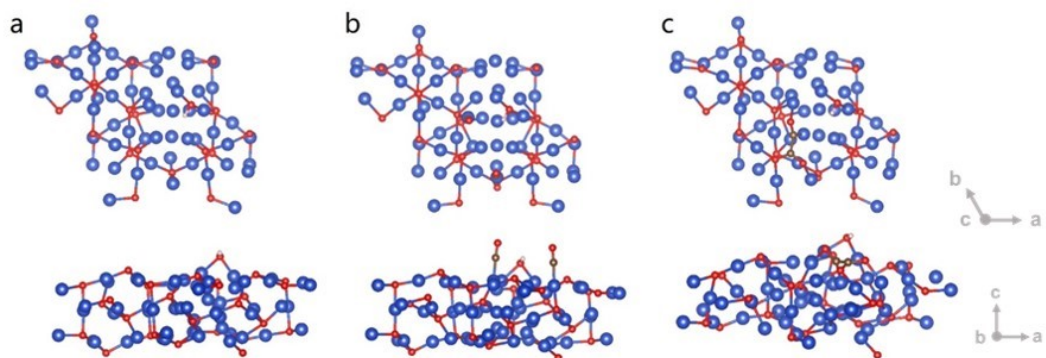


**Figure S40.** The DFT calculation models of (a)  $\text{CuO}_x+\text{OH}^-$  and  $\text{CuO}_x+\text{OH}^-$  for (b)  $\text{CO}^*+\text{CO}^*$  formation and (b)  $\text{O}^*\text{CCO}$  formation.

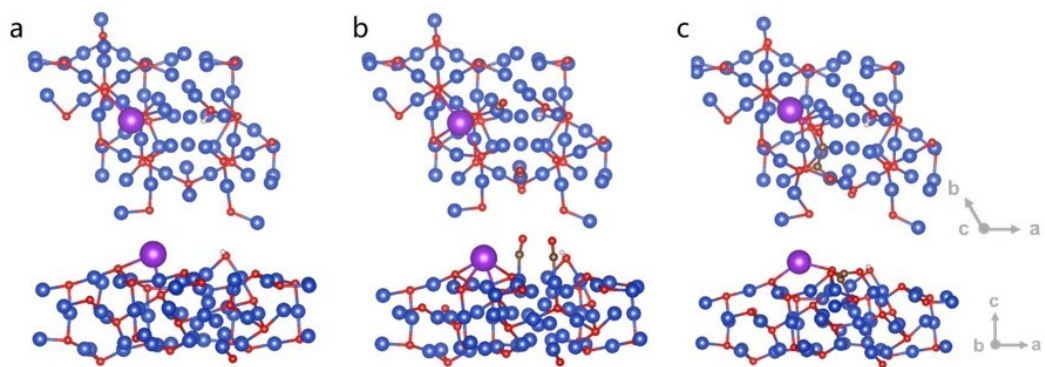


**Figure S41.** The DFT calculation models of (a)  $\text{CuO}_x + \text{K}^+ \text{OH}^-$  and  $\text{CuO}_x + \text{K}^+ \text{OH}^-$  for (b)  $\text{CO}^* + \text{CO}^*$  formation and (c)  $\text{O}^* \text{CCO}$  formation.

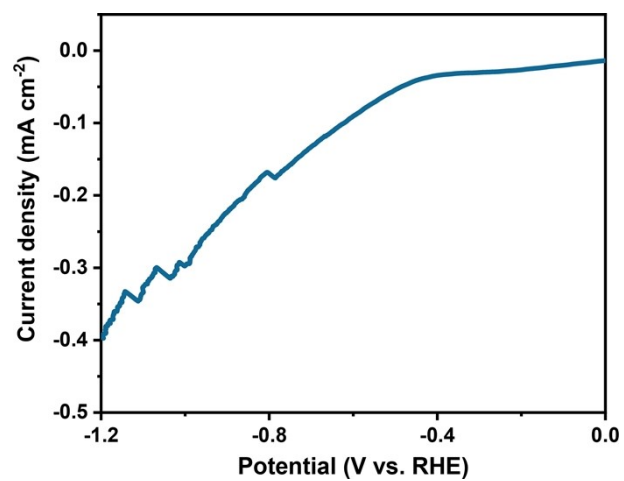


**Figure S42.** LSV curves for CuO<sub>x</sub>-dendrites in an acidic medium (pH=1.6).

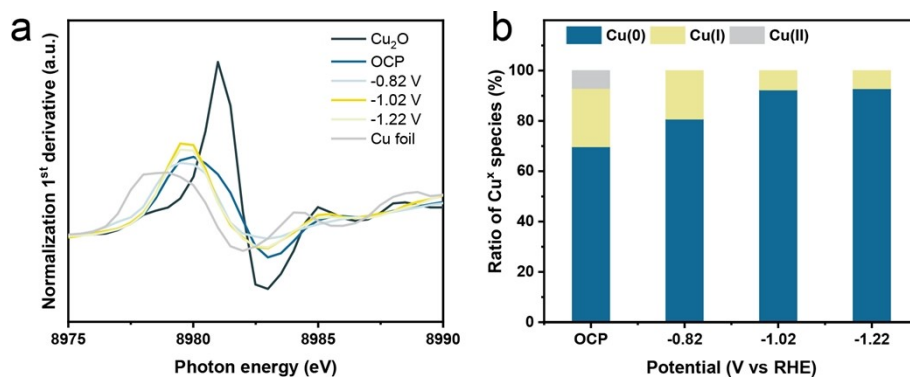


**Figure S43.** (a) Operando Cu K-edge first derivative XANES of  $\text{CuO}_x$ -dendrites during the  $\text{CO}_2\text{R}$  in an acidic medium ( $\text{pH}=1.6$ ). (b) The calculated ratio of  $\text{Cu}^x$  species concerning potential.

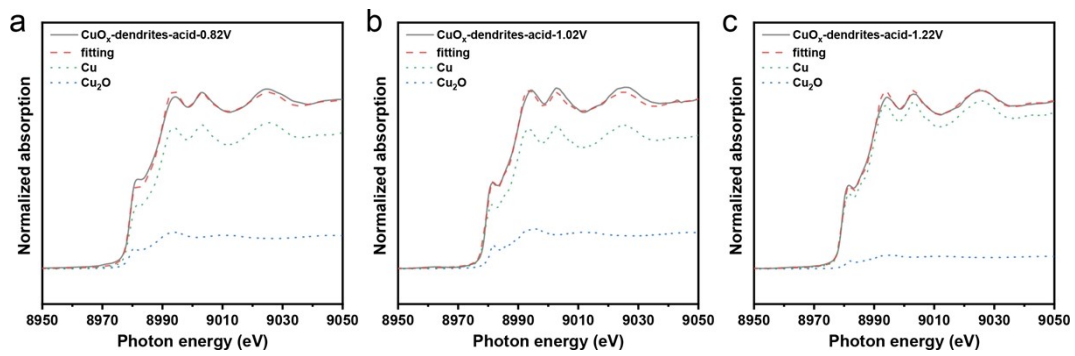


**Figure S44.** LCF of CuO<sub>x</sub>-dendrites at -0.82 (a), -1.02 (b), and -1.22 V<sub>RHE</sub> (c) in an acidic medium.

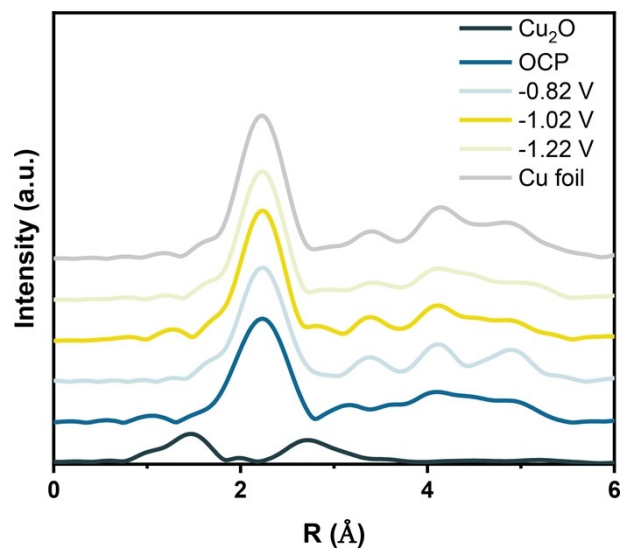


**Figure S45.** Fourier-transform  $k^2$ -weighted EXAFS spectra of  $\text{CuO}_x$ -dendrites during the  $\text{CO}_2\text{R}$  in an acidic medium (pH=1.6).

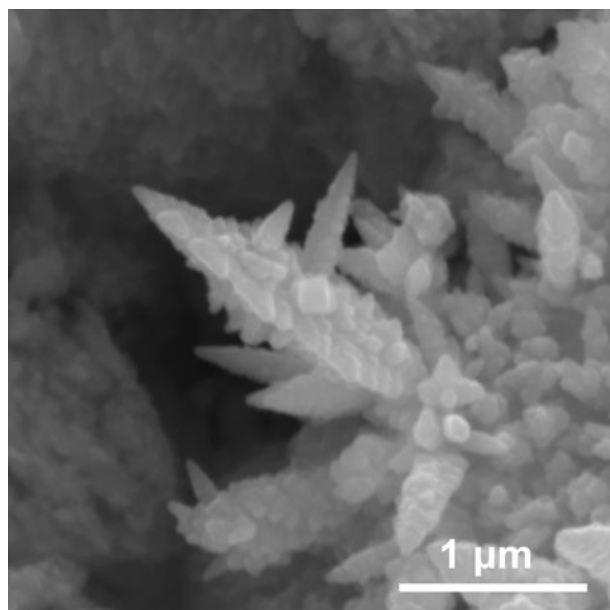


**Figure S46.** SEM image of CuO<sub>x</sub>-dendrites after CO<sub>2</sub>R in an acidic medium (pH=1.6).

**Table S1.** Faradaic efficiency (FE) values of all products in CO<sub>2</sub>R on CuO<sub>x</sub>-dendrites catalysts in an alkaline medium.

Current density (A cm <sup>-2</sup> )	Faradaic efficiency (%)							
	C <sub>2</sub> H <sub>4</sub>	EtOH	AcO <sup>-</sup>	n-PrOH	HCOO <sup>-</sup>	CH <sub>4</sub>	CO	H <sub>2</sub>
0.4	45.7±2.1	4.6±1.0	1.2±0.1	1.7±0.2	2.1±0.2	0.2	31.0±3.0	11.7±1.1
0.5	51.5±2.4	6.6±0.4	1.3±0.2	2.3±0.3	2.9±0.3	0.2	20.5±2.4	13.7±1.3
0.6	56.1±2.6	5.0±0.7	0.9±0.1	2.1±0.2	2.0±0.3	0.2	18.6±2.7	12.6±2.2
0.7	64.2±3.2	7.8±0.3	1.9±0.1	2.1±0.2	1.7±0.2	0.2	9.1±2.6	12.8±1.6
0.9	73.9±2.1	5.6±0.5	1.7±0.2	1.3±0.1	0.5±0.1	0.2	6.8±3.0	10.9±1.7
1.0	68.9±1.8	5.3±0.4	1.3±0.2	2.0±0.2	0.4±0.1	0.4	6.6±2.8	14.6±2.8
1.2	55.6±5.8	6.7±0.4	2.4±0.3	3.0±0.3	2.0±0.5	0.9	5.5±2.8	25.6±5.6

**Table S2.** Comparison of CO<sub>2</sub>R to ethylene performance with state-of-the-art catalysts.

Catalyst	Potential (V <sub>RHE</sub> )	FE <sub>C<sub>2</sub>H<sub>4</sub></sub> (%)	J <sub>C<sub>2</sub>H<sub>4</sub></sub> (mA cm <sup>-2</sup> )	Ref.
CuO <sub>x</sub> -dendrites	-2.35	73.9	665.1	This work
Cu-arylpyridiniums	-3.3	72	230.4	12
PFSA-Cu	-2.3	72	230.4	13
CuO-Al <sub>2</sub> CuO <sub>4</sub>	-3.26	70.1	421	14

**Table S3.** Structural parameters of CuO<sub>x</sub>-dendrites, CuO<sub>x</sub>-particles, and reference samples that are extracted from the Cu K-edge EXAFS fitting.

Sample	Shell	N	R(Å)	ΔE <sub>0</sub> (eV)	Δσ <sup>2</sup> *10 <sup>3</sup> (Å <sup>2</sup> )	R-factor (%)
Cu foil	Cu-Cu	12	2.55	/	/	/
CuO	Cu-O1	4	1.96	/	/	/
	Cu-O2	2	2.78	/	/	/
Cu <sub>2</sub> O	Cu-O	2	1.88	/	/	/
	Cu-Cu	8	3.01	/	/	/
CuO <sub>x</sub> -dendrites- OCP	Cu-O	0.7±0.3	1.91±0.03	-2.2±6.5	13.3±1.1	1.7
	Cu-Cu	6.5±0.3	2.52±0.04	-5.6±1.4	5.6±5.1	
CuO <sub>x</sub> -dendrites- 0.6V	Cu-O	0.4±0.1	1.94±0.02	-10(set)	8.2±1.3	0.3
	Cu-Cu	8.3±0.5	2.53±0.02	3.4±1.0	8.3±0.9	
CuO <sub>x</sub> -dendrites- 0.8V	Cu-O	0.3±0.1	1.91±0.04	6.1±4.3	16.7±7.3	0.2
	Cu-Cu	9.0±0.7	2.53±0.01	3.0±1.5	7.5±1.0	
CuO <sub>x</sub> -dendrites- 1.0V	Cu-O	0.2±0.1	1.93±0.02	4.3±1.8	9.1±0.2	0.5
	Cu-Cu	9.3±0.6	2.53±0.03	2.1±1.3	7.8±1.1	
CuO <sub>x</sub> -particles- 0.4V	Cu-O	<0.3	/	/	/	0.8
	Cu-Cu	9.9±0.7	2.54±0.01	4.1±0.8	8.3±0.6	
CuO <sub>x</sub> -particles- 0.6V	Cu-O	<0.3	/	/	/	1.5
	Cu-Cu	10.1±1.1	2.54±0.02	3.8±1.1	8.5±0.9	
CuO <sub>x</sub> -particles- 0.8V	Cu-O	<0.3	/	/	/	1.3
	Cu-Cu	9.9±0.9	2.54±0.01	4.5±1.0	8.4±0.8	

Δk = 3.0 – 11.5 Å<sup>-1</sup>, Δr = 1.1 – 2.7 Å.

N, coordination number; R, the distance between the absorber and backscatter atoms; ΔE<sub>0</sub>, inner potential correction; σ<sup>2</sup>, Debye-Waller factor to account for both thermal and structural disorders;

The obtained S<sub>0</sub><sup>2</sup> of Cu foil was 0.877 and it was fixed in the subsequent fitting of Cu K-edge data for the catalyst.

**Table S4.** DFT total energies ( $E_{\text{DFT}}$ ), zero-point energies ( $E_{\text{ZPE}}$ ), entropies multiplied by temperature ( $T\Delta S$ ,  $T = 298.15$  K), free energies ( $G$ ) and relative free energies ( $\Delta G$ ) of  $\text{CO}_2$  reduction reaction intermediates.

	$E_{\text{DFT}}$ (eV)	$E_{\text{ZPE}}$ (eV)	$T\Delta S$ (eV)	$G$ (eV)	$\Delta G$ (eV)
$\text{CuO}_x$	-286.74				
$\text{CO}^* + \text{CO}^*$	-324.07	393.29	356.45	-324.03	
$\text{O}^*\text{CCO}$	-323.03	466.83	164.41	-322.73	1.30
$\text{CuO}_x + \text{K}^+$	-295.30				
$\text{CO}^* + \text{CO}^*$	-327.57	193.26	343.78	-327.72	
$\text{O}^*\text{CCO}$	-326.74	468.22	167.23	-326.44	1.28
$\text{CuO}_x + \text{OH}^-$	-302.88				
$\text{CO}^* + \text{CO}^*$	-335.52	407.26	290.91	-335.40	
$\text{O}^*\text{CCO}$	-334.28	463.84	171.13	-333.99	1.41
$\text{CuO}_x + \text{K}^+ + \text{OH}^-$	-305.91				
$\text{CO}^* + \text{CO}^*$	-338.21	396.50	281.95	-338.09	
$\text{O}^*\text{CCO}$	-337.80	470.21	154.42	-337.48	0.61

**Table S5.** Faradaic efficiency (FE) values of all products in CO<sub>2</sub>R on CuO<sub>x</sub>-dendrites catalysts in an acidic medium.

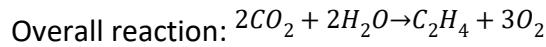
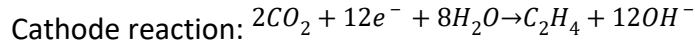
Current density (A cm <sup>-2</sup> )	Faradaic efficiency (%)							
	C <sub>2</sub> H <sub>4</sub>	EtOH	AcOH	n-PrOH	HCOOH	CH <sub>4</sub>	CO	H <sub>2</sub>
0.4	42.1±2.1	11.5±1.5	2.1±0.2	5.3±0.3	9.6±1.0	0.1	14.2±0.5	10.2±0.8
0.5	44.8±2.2	16.6±1.7	2.2±0.2	6.0±0.9	6.2±0.6	0.1	12.0±0.2	10.2±1.6
0.6	52.5±4.1	14.3±0.4	2.6±0.3	3.0±0.5	4.3±0.8	0.2	11.0±0.3	10.0±0.4
0.7	57.1±3.3	14.2±0.6	1.9±0.2	3.8±0.4	2.4±0.2	0.6	9.8±0.7	10.1±1.8
0.8	55.1±3.9	15.8±1.6	2.1±0.2	3.9±0.3	1.7±0.2	0.7	8.3±0.9	12.8±0.3
0.9	47.1±1.8	14.3±1.2	7.7±0.9	2.1±0.3	2.0±0.3	3.2	6.3±1.1	15.5±1.2

**Table S6.** pH of catholyte and anolyte before and after CO<sub>2</sub>R at 400 mA cm<sup>-2</sup>.

Electrolyte	Catholyte		Anolyte	
pH 14	0 h	14.01	0 h	14.01
	1 h	14.00	1 h	13.98
	2 h	14.03	2 h	13.99
	3 h	13.98	3 h	14.01
pH 1.6	0 h	1.60	0 h	1.60
	1 h	1.61	1 h	1.58
	2 h	1.63	2 h	1.57
	3 h	1.65	3 h	1.57

**Supplementary Note 1:** We considered the costs of producing 100 tons of ethylene per day. We use an experimentally potential derived flow cell voltage of -1.12 V and plus the theoretical OER potential 1.23 V, the total cell voltage is more than 2.35 V. And an experimentally derived total current density of 900 mA cm<sup>-2</sup> for a prospective industrial electrolyzer.

For the formation of ethylene from CO<sub>2</sub>, the chemical equation is:



Therefore, producing 1 mol of ethylene (C<sub>2</sub>H<sub>4</sub>) requires 2 mol CO<sub>2</sub> and 2 mol H<sub>2</sub>O. However, the selectivity of CO<sub>2</sub>-to-ethylene is less than 100%, so more than 2 mol of CO<sub>2</sub> is needed.

The cost of ethylene includes the following costs:

$$\begin{aligned} \text{Cost}_{\text{ethylene}} &= \text{Cost}_{\text{electricity}} + \text{Cost}_{\text{electrolyzer}} + \text{Cost}_{\text{catalyst and membrane}} + \text{Cost}_{\text{gas separation}} \\ &+ \text{Cost}_{\text{electrolyte}} + \text{Cost}_{\text{operation + installation}} + \text{BOP} \end{aligned}$$

### Electricity:

The production rate of ethylene in moles per second ( $Q$ ) is:

$$Q = C_2H_4 \text{ production (mol/s)} = \frac{C_2H_4 \text{ production}}{M_{C_2H_4}} = 41.34 \text{ mol/s}$$

Considering the loss of electrons, the current needed to produce ethylene at the target production rate ( $I_{\text{total}}$ ):

$$I_{\text{total}}(A) = \frac{C_2H_4 \text{ production} * n * F}{FE_{C_2H_4}} = 6476983.5 A$$

Where  $n$  correspond to the number of electrons transferred for C<sub>2</sub>H<sub>4</sub>,  $F$  is Faraday's constant (96485 C·mol<sup>-1</sup>). The FE<sub>C<sub>2</sub>H<sub>4</sub></sub> is 73.9% at 900 mA cm<sup>-2</sup>.

The power consumed with the total cell voltage 2.35 V:

$$\text{Power (kW)} = I_{\text{total}}(A) * V_{\text{cell}}(V) = 152209.1 \text{ kW}$$

The cost per ton of ethylene with 0.01\$/kWh<sup>16</sup>(*Nat. Energy* 2022, 7, 170-176) for 24-hour consumption:

$$Cost_{electricity} (\$/ton) = \frac{Power * 24 \text{ hr} * 0.01 \$/kWh}{C_2H_4 \text{ production}} = \$365.30/ton$$

### Electrolyzer:

The cost of the electrolyzer from the reference at 400 mA cm<sup>-2</sup> current density is 450 \$/kW<sup>17-19</sup> (*Nature* 2023, 617, 724-729; *Fuel Cell Seminar & Energy Exposition* 2017; *ACS Energy Lett.* 2021, 6, 997-1002). Thus, the total cost of the electrolyzer:

$$Cost_{total \text{ electrolyzer}} = Power * Cost_{reference} * \frac{reference \text{ current density}}{input \text{ current density}} = \$30441822.5$$

This technique of converting long-term investments into daily costs is used for all capital costs and uses a capital recovery factor (CRF) based on the discount rate *i* (7%) and the lifetime of the material (20 years)<sup>16-17</sup>(*Nature* 2023, 617, 724-729; *Nat. Energy* 2022, 7, 170-176).

$$CRF_{electrolyzer} = \frac{i(1+i)^{life \text{ time}}}{(1+i)^{life \text{ time}} - 1} = 0.094393$$

The total electrolyzer capital cost by the CRF and divide it by the number of days the plant operates and the daily ethylene production. For all calculations, we assume that the factory has a capacity factor (*CF*) of 0.9<sup>16-17</sup> (*Nature* 2023, 617, 724-729; *Nat. Energy* 2022, 7, 170-176):

$$Cost_{electrolyzer} (\$/ton) = \frac{CRF_{electrolyzer} * Cost_{total \text{ electrolyzer}}}{CF * 365 * C_2H_4 \text{ production}} = \$87.47/ton$$

### Catalyst and Membrane:

Assume 5% of the electrolyzer cost for 5 years of catalyst/membrane lifetime:

$$CRF_{catalyst \text{ and membrane}} = 0.24389$$

$$Cost_{catalyst \text{ and membrane}} = \frac{CRF_{catalyst \text{ and membrane}} * Cost_{total \text{ electrolyzer}} * 5\%}{CF * 365 * C_2H_4 \text{ production}} = \$11.30/ton$$

### Gas Separation:

Gaseous side products (H<sub>2</sub>) are separated from the CO<sub>2</sub> outlet stream to enable the recirculation of unreacted CO<sub>2</sub>. We calculate gaseous separation costs using estimates from a reference pressure-swing adsorption (PSA) system.

$$C_2H_4 \text{ Flow rate} \left( \frac{m^3}{h} \right) = \frac{C_2H_4 \text{ production rate} * R * T}{P} = 3639.5 \left( \frac{m^3}{h} \right)$$

The theoretical limit single-pass carbon efficiency (SPCE) for alkaline systems is 25%<sup>18</sup>(*Science* 2021, 372, 1074-1078).

$$\text{Output } CO_2 \text{ Flow rate } \left( \frac{m^3}{h} \right) = \frac{C_2H_4 \text{ production rate} * (1 - SPCE)}{SPCE} = 10918.5 \left( \frac{m^3}{h} \right)$$

$$\text{Output } H_2 \text{ Flow rate } \left( \frac{m^3}{h} \right) = \frac{\text{Total current} * FE_{H_2} * R * T}{F * 2 * P} = 3033.0 \left( \frac{m^3}{h} \right)$$

Where R is universal gas constant, T is room temperature and P is ordinary pressure.

$$\begin{aligned} \text{The total Flow rate } \left( \frac{m^3}{h} \right) &= C_2H_4 \text{ Flow rate } \left( \frac{m^3}{h} \right) + \text{Output } CO_2 \text{ Flow rate } \left( \frac{m^3}{h} \right) + \text{Output } H_2 \text{ Flow rate} \\ \left( \frac{m^3}{h} \right) &= 17591.0 \left( \frac{m^3}{h} \right) \end{aligned}$$

$$\begin{aligned} \text{Cost}_{\text{Gas Separation Operation}} \left( \frac{\$}{\text{ton}} \right) &= \frac{\text{total flow rate} * \text{reference PSA cost} * \text{electricity price}}{\text{target output production}} = \$10.55/\text{ton} \end{aligned}$$

$$\begin{aligned} \text{Cost}_{\text{Gas Separation Capital}} \left( \frac{\$}{\text{ton}} \right) &= \frac{\text{reference PSA capital cost} * \left( \frac{\text{total flow rate}}{\text{reference capacity}} \right)^{\text{scaling factor}} * CRF}{\text{capacity factor} * 365 * \text{target output production}} \\ &= \frac{\$1989043 * \left( \frac{16628.4}{1000} \right)^{0.7} * 0.094}{0.9 * 365 * 100} = \$42.36/\text{ton} \end{aligned}$$

$$\text{Cost}_{\text{Gas Separation}} = \text{Cost}_{\text{Gas Separation Operation}} + \text{Cost}_{\text{Gas Separation Capital}} = \$52.91/\text{ton}$$

Where reference PSA cost is 0.25 kWh/m<sup>3</sup>, reference PSA capital cost is \$1989043, reference PSA capacity is 1000m<sup>3</sup>/h, PSA capacity scaling factor is 0.7<sup>19-20</sup> (*Ind. Eng. Chem. Res.* 2018, 57, 2165-2177; *Nat. Sustain.* 2021, 4, 911-919).

### Input CO<sub>2</sub>:

Producing 1 mol of ethylene (C<sub>2</sub>H<sub>4</sub>) requires 2 mol CO<sub>2</sub>. The total input CO<sub>2</sub> is 314.3 tons to produce 100 tons of ethylene. And the market price for CO<sub>2</sub> is \$30/ton.

$$\text{Cost}_{\text{input } CO_2} = \$94.28/\text{ton}$$

### Electrolyte cost:

Our electrolyte is 1.0 M KOH. By using a fixed volume ratio of 100 L of electrolyte per square meter of electrolyzer, we can find the total volume of electrolyte needed.

$$\text{Volume}_{\text{electrolyte}} (L) = \text{Surface area}_{\text{electrolyzer}} (m^2) * 100 \left( \frac{L}{m^2} \right) = 830896.2 L$$

$$Mass_{salt}(g) = molarity_{salt} \left( \frac{mol}{L} \right) * Volume_{electrolyte}(L) * molecular\ wight \left( \frac{g}{mol} \right) = 46530189.0\ g$$

$$Cost_{total\ electrolyte} = Mass_{salt}(ton) * price_{salt} \left( \frac{\$}{ton} \right) + Volume_{water}(L) * price_{water} \left( \frac{\$}{ton} \right) = \$40913.$$

3

To obtain the cost per ton of ethylene, we calculate the new CRF (1.07) by assuming an electrolyte lifetime of one year. Electrolyte costs per ton of ethylene:

$$Cost_{total\ electrolyte} \left( \frac{\$}{ton} \right) = \frac{CRF * Cost_{total\ electrolyte}}{CF * 365 * C_2H_4\ production} = \$1.33/ton$$

### Balance of Plant and Installation:

All capital costs are scaled to estimate the price of peripheral equipment around the electrolyzer and separation units. We assume a balance of plants (BOP) of 50% and a Lang factor of  $1^{16-17, 21}$  (*Nature* 2023, 617, 724-729; *Joule* 2021, 5, 706-719; *Nat. Energy* 2022, 7, 170-176). To find our total capital costs, we sum the costs of the electrolyzer, membrane & catalyst, and cathode separation capital.

$$Cost_{total\ capital} \left( \frac{\$}{ton} \right) = Electrolyzer\ cost + Catalyst\ cost + PSA\ capital\ cost = \$208.2/ton$$

$$Cost_{installation} \left( \frac{\$}{ton} \right) = Lang\ Factor * Cost_{total\ capital} = \$208.2/ton$$

$$BOP \left( \frac{\$}{ton} \right) = BOP\ Factor * Cost_{total\ capital} = \$104.1/ton$$

### Other operating costs:

To consider the additional operating costs associated with operating the factory (such as labor and maintenance), we have added an additional cost equal to 10% of the electricity cost:

$$Cost_{Other\ operation} \left( \frac{\$}{ton} \right) = Cost_{electricity} \left( \frac{\$}{ton} \right) * 0.1 = \$36.53/ton$$

### Total cost for one ton of ethylene:

By summing all the above costs, the cost to produce one ton of ethylene in an electrolyzer:

$$\begin{aligned} Cost_{ethylene} &= Cost_{electricity} + Cost_{electrolyzer} + Cost_{catalyst\ and\ membrane} + Cost_{gas\ separation} + Cost_{CO_2} \\ &\quad + Cost_{electrolyte} + Cost_{operation + installation} + BOP \\ &= \frac{\$365.30}{ton} + \frac{\$87.47}{ton} + \frac{\$11.70}{ton} + \frac{\$52.91}{ton} + \frac{\$94.28}{ton} + \frac{\$1.33}{ton} + \frac{\$208.2}{ton} + \frac{\$36.53}{ton} + \frac{\$104.1}{ton} \\ &= \$961.82/ton \end{aligned}$$



**Supplementary Note 2:** Although the in situ Raman cell achieved the separation of gas and liquid in CO<sub>2</sub>R, the lower current density was conducted compared with the flow cell due to the limitations of ionic and electronic transfer. To illustrate the effect of the local microenvironment, in situ, Raman tests with control galvanostatic of CuO<sub>x</sub>-dendrites and CuO<sub>x</sub>-particles were conducted for comparison. The potential which was obtained by in situ Raman test refers to the corresponding current density by the flow cell. In this regard, the potential and corresponding current density were listed in the following table.

	Potential (V vs RHE)	Current density (mA cm <sup>-2</sup> )
CuO <sub>x</sub> -dendrites	-0.47	70
	-0.67	220
	-0.87	430
	-0.97	570
CuO <sub>x</sub> -particles	-0.49	70
	-0.89	220
	-1.29	430
	-1.59	570

## Supplementary References

- (1). Ravel, B.; Newville, M. *J. Synchrotron Radiat.* 2005, **12**, 537-541.
- (2). Tröger, L.; Arvanitis, D.; Baberschke, K.; Michaelis, H.; Grimm, U.; Zschech, E. *Phys. Rev. B* 1992, **46**, 3283-3289.
- (3). Kresse, G.; Furthmüller, J. *Comput. Mater. Sci.* 1996, **6**, 15-50.
- (4). Kresse, G.; Furthmüller, J. *Phys. Rev. B* 1996, **54**, 11169-11186.
- (5). Perdew, J. P.; Burke, K.; Ernzerhof, M. *Phys. Rev. Lett.* 1996, **77**, 3865-3868.
- (6). Blöchl, P. E. *Phys. Rev. B* 1994, **50**, 17953-17979.
- (7). Kresse, G.; Joubert, D. *Phys. Rev. B* 1999, **59**, 1758-1775.
- (8). Monkhorst, H. J.; Pack, J. D. *Phys. Rev. B* 1976, **13**, 5188-5192.
- (9). Nørskov, J. K.; Rossmeisl, J.; Logadottir, A.; Lindqvist, L.; Kitchin, J. R.; Bligaard, T.; Jónsson, H. *J. Phys. Chem. B* 2004, **108**, 17886-17892.
- (10). Cejka, J.; Sejkora, J.; Jebava, I.; Xi, Y.; Couperthwaite, S.J.; Frost, R.L. *Acta A Mol. Biomol. Spectrosc.* 2013, **108**, 171-176.
- (11). Yu, P.; Shen, Y. *Phys. Rev. B* 1975, **12**, 1377-1394.
- (12). Li, F.; Thevenon, A.; Rosas-Hernandez, A.; Wang, Z.; Li, Y.; Gabardo, C. M.; Ozden, A.; Dinh, C. T.; Li, J.; Wang, Y.; Edwards, J. P.; Xu, Y.; McCallum, C.; Tao, L.; Liang, Z. Q.; Luo, M.; Wang, X.; Li, H.; O'Brien, C. P.; Tan, C. S.; Nam, D. H.; Quintero-Bermudez, R.; Zhuang, T. T.; Li, Y. C.; Han, Z.; Britt, R. D.; Sinton, D.; Agapie, T.; Peters, J. C.; Sargent, E. H. *Nature* 2020, **577**, 509-513.
- (13). Zhao, Y.; Hao, L.; Ozden, A.; Liu, S.; Miao, R. K.; Ou, P.; Alkayyali, T.; Zhang, S.; Ning, J.; Liang, Y.; Xu, Y.; Fan, M.; Chen, Y.; Huang, J. E.; Xie, K.; Zhang, J.; O'Brien, C. P.;

- Li, F.; Sargent, E. H.; Sinton, D. *Nat. Synth.* 2023, **2**, 403-412.
- (14). Sultan, S.; Lee, H.; Park, S.; Kim, M. M.; Yoon, A.; Choi, H.; Kong, T.-H.; Koe, Y.-J.; Oh, H.-S.; Lee, Z.; Kim, H.; Kim, W.; Kwon, Y. *Energy Environ. Sci.* 2022, **15**, 2397-2409.
- (15). Mu, S.; Lu, H.; Wu, Q.; Li, L.; Zhao, R.; Long, C.; Cui, C. *Nat. Commun.* 2022, **13**, 3694.
- (16). Jin, J.; Wicks, J.; Min, Q.; Li, J.; Hu, Y.; Ma, J.; Wang, Y.; Jiang, Z.; Xu, Y.; Lu, R.; Si, G.; Papangelakis, P.; Shakouri, M.; Xiao, Q.; Ou, P.; Wang, X.; Chen, Z.; Zhang, W.; Yu, K.; Song, J.; Jiang, X.; Qiu, P.; Lou, Y.; Wu, D.; Mao, Y.; Ozden, A.; Wang, C.; Xia, B.; Hu, X.; Dravid, V. P.; Yiu, Y.; Sham, T.; Wang, Z.; Sinton, D.; Mai, L.; Sargent, E. H.; Pang, Y. *Nature* 2023, **617**, 724-729.
- (17). Wang, X.; Ou, P.; Ozden, A.; Hung, S.; Tam, J.; Gabardo, C. M.; Howe, J. Y.; Sisler, J.; Bertens, K.; Arquer, F. P. G.; Miao, R. L.; O'Brien, C. P.; Wang, Z.; Abed, J.; Rasouli, A. S.; Sun, M.; Alexander, H. I.; Sinton, D.; Sargent, E. H. *Nat. Energy* 2022, **7**, 170-176.
- (18). Ruth, M.; Mayyas, A.; Mann, M., *Fuel Cell Seminar & Energy Exposition* 2017.
- (19). Sisler, J.; Khan, S.; Ip, A. H.; Schreiber, M. W.; Jaffer, S. A.; Bobicki, E. R.; Dinh, C.-T.; Sargent, E. H., *ACS Energy Lett.* 2021, **6**, 997-1002.
- (20). Huang, J. E.; Li, F.; Ozden, A.; Rasouli, A. S.; Arquer, F. P.; Liu, S.; Zhang, S.; Luo, M.; Wang, X.; Lum, Y.; Xu, Y.; Bertens, K.; Miao, R. K.; Dinh, C.; Sinton, D.; Sargent, E. H. *Science* 2021, **372**, 1074-1078.
- (21). Ozden, A.; Wang, Y.; Li, F.; Luo, M.; Sisler, J.; Thevenon, A.; Rosas-Hernández, A.; Burdyny, T.; Lum, Y.; Yadegari, H.; Agapie, T.; Peters, J. C.; Sargent, E. H.; Sinton, D., *Joule* 2021, **5**, 706-719.